This article was downloaded by: [the LANL Research Library]
On: 21 December 2011, At: 12:39
Publisher: Taylor & Francis
Informa Ltd Registered in England and Wales Registered Number: 1072954 Registered office: Mortimer House, 37-41 Mortimer Street, London W1T 3JH, UK

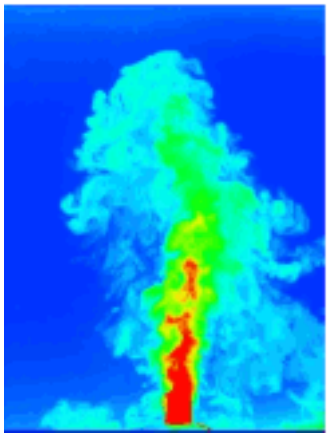

Journal of Turbulence
Publication details, including instructions for authors and subscription information:
http://www.tandfonline.com/loi/tjot20

Application of a second-moment closure model to mixing processes involving multicomponent miscible fluids

John D. Schwarzkopf [a], Daniel Livescu [a], Robert A. Gore [a], Rick M. Rauenzahn [a] & J. Raymond Ristorcelli [a]
[a] Los Alamos National Laboratory, Los Alamos, NM, 87545, USA

Available online: 21 Dec 2011

To cite this article: John D. Schwarzkopf, Daniel Livescu, Robert A. Gore, Rick M. Rauenzahn & J. Raymond Ristorcelli (2011): Application of a second-moment closure model to mixing processes involving multicomponent miscible fluids, Journal of Turbulence, 12, N49

To link to this article: http://dx.doi.org/10.1080/14685248.2011.633084

PLEASE SCROLL DOWN FOR ARTICLE

Full terms and conditions of use: http://www.tandfonline.com/page/terms-and-conditions

This article may be used for research, teaching, and private study purposes. Any substantial or systematic reproduction, redistribution, reselling, loan, sub-licensing, systematic supply, or distribution in any form to anyone is expressly forbidden.

The publisher does not give any warranty express or implied or make any representation that the contents will be complete or accurate or up to date. The accuracy of any instructions, formulae, and drug doses should be independently verified with primary sources. The publisher shall not be liable for any loss, actions, claims, proceedings, demand, or costs or damages whatsoever or howsoever caused arising directly or indirectly in connection with or arising out of the use of this material.

Journal of Turbulence
Vol. 12, No. 49, 2011, 1–35

Taylor & Francis
Taylor & Francis Group

Application of a second-moment closure model to mixing processes involving multicomponent miscible fluids

John D. Schwarzkopf*, Daniel Livescu, Robert A. Gore, Rick M. Rauenzahn and J. Raymond Ristorcelli

Los Alamos National Laboratory, Los Alamos, NM 87545, USA

(*Received 1 June 2011; final version received 3 October 2011*)

A second-moment closure model is proposed for describing turbulence quantities in flows where large density fluctuations can arise due to mixing between different density fluids, in addition to compressibility or temperature effects. The turbulence closures used in this study are an extension of those proposed by Besnard et al., which include closures for the turbulence mass flux and density-specific-volume covariance. Current engineering models developed to capture these extended effects due to density variations are scarce and/or greatly simplified. In the present model, the density effects are included and the results are compared to direct numerical simulations (DNS) and experimental data for flow instabilities with low to moderate density differences. The quantities compared include Reynolds stresses, turbulent mass flux, mixture density, density-specific-volume covariance, turbulent length scale, turbulence and material mix time scales, turbulence dissipation, and mix widths and/or growth rates. These comparisons are made within the framework of three very different classes of flows: shear-driven, Rayleigh–Taylor and Richtmyer–Meshkov instabilities. Overall, reasonable agreement is seen between experiments, DNS, and averaging models.

Keywords: turbulence; mixing; variable density; Reynolds stress; closure model; Rayleigh–Taylor; Richtmyer–Meshkov; direct numerical simulation; shocks; Favre average; compressible flows; density fluctuations

Downloaded by [the LANL Research Library] at 12:39 21 December 2011

1. Introduction

Density fluctuations in turbulent flows are encountered in many practical applications, ranging from Inertial Confinement Fusion (ICF), atmospheric and oceanic flows, astrophysics, and many flows of engineering interest. In general, turbulent density fluctuations have been studied in conjunction with compressibility effects (e.g., in aeronautics) or as a result of temperature changes (e.g., in combustion). Such flows have been the subject of numerous fundamental turbulence studies and many modeling strategies now exist. Nevertheless, large density variations can also occur due to mixing of different density fluids. In this case, fundamental turbulence studies as well as specific engineering models are scarce.

To distinguish from other effects, variable-density (VD) flows are described as having large density variations that arise due to mixing between different density fluids. The differential acceleration effects in VD flows are usually characterized by the Atwood number

*Corresponding author. Email: jschwar@lanl.gov

ISSN: 1468-5248 online only
© 2011 Taylor & Francis
http://dx.doi.org/10.1080/14685248.2011.633084
http://www.tandfonline.com

(*A*):

$$A \equiv \frac{\rho_{\max} - \rho_{\min}}{\rho_{\max} + \rho_{\min}}, \tag{1}$$

where the Atwood number is bounded between 0 and 1. At low A, the densities are commensurate and the density fluctuations can be neglected in the advective terms. At high A, the density fluctuations can no longer be neglected in the advective terms and higher order nonlinearities arise in the governing equations. For example, for air interpenetrating helium, for which the density ratio is $\approx$7, the Atwood number is $A\approx$0.75. For air and hydrogen, $A\approx$0.85. Similar Atwood numbers occur for mixing between liquid hydrocarbons and air.

There have been several in-depth studies on the nature of VD turbulent flows. Livescu and Ristorcelli [1] point out that in VD flows, even if the fluids participating in the mixing are individually incompressible, the velocity is not solenoidal and the specific volume becomes a dependent variable. They also showed that the density-specific-volume covariance can be expressed in the form of a series of the density PDF moments:

$$\overline{\upsilon'\rho'} = -\frac{\overline{\rho'^2}}{\bar{\rho}^2}\left[1 - i_\rho \frac{\overline{\rho'^3}}{(\overline{\rho'^2})^{3/2}} + i_\rho^2 \frac{\overline{\rho'^4}}{(\overline{\rho'^2})^2} - i_\rho^3 \frac{\overline{\rho'^5}}{(\overline{\rho'^2})^{5/2}} + \ldots\right], \tag{2}$$

where $i_\rho = \rho_{\rm rms}/\bar{\rho}$. In the Boussinesq limit (i.e., in the range of $0 \le A \le 0.05$, [1], [2]), higher order effects can be neglected, i.e., $\overline{\upsilon'\rho'} \approx -\overline{\rho'^2}/\bar{\rho}^2$, or $i_\rho = 0$. Second moment models have been developed around this assumption, yet applied to moderate Atwood number turbulent flows. However, this assumption is not valid at higher Atwood numbers. Using direct numerical simulations (DNS), Livescu et al. [2] showed that even for a moderate Atwood of 0.5, $\overline{\upsilon'\rho'}/(-\overline{\rho'^2}/\bar{\rho}^2) \neq 1$, but varied by as much as 25% near the edges of the mixing zone. Livescu et al. [3] also highlight the importance of using the density-specific-volume covariance, which appears in the moment equations in the VD case, as opposed to the density variance, which appears in the moment equations for the Boussinesq case.

Although DNS is a useful tool for investigating flow and/or mixing physics, the computational power required to apply it to engineering problems can be enormous. As an interim solution, Favre or ensemble averaging provides an avenue by which engineers can obtain reasonable results in a short period of time. Most engineering models addressing VD turbulence are simple extensions of compressible turbulence models (e.g., [4], etc.), using the density variance as a prognostic variable, so that they are appropriate only in the Boussinesq limit. One exception is the system of Favre-averaged equations to simulate VD-compressible turbulent flows, developed by Besnard et al. [5]. Their approach of modeling the turbulent moments in a mixture of several fluids presented several new quantities, not addressed in previous studies. These include the turbulent mass flux ($\bar{\rho}a_i = \overline{\rho' u_i'}$) and the density-specific-volume covariance ($b = -\overline{\rho'\upsilon'}$), where υ' is the fluctuation of the specific volume.

Banjeree et al. [6] discuss a restriction to the work of Besnard et al. [5] for the incompressible case and a simple expression for *b,* strictly valid for immiscible materials. Their model (BHR *k-S-a*) uses the turbulent viscosity hypothesis to model the components of the Reynolds stress tensor, which assumes isotropy in regions where there are no mean velocity gradients. In addition, the turbulent diffusion terms were also modeled using the isotropic turbulent viscosity. These simple models did compare well with the experimental data, but they are missing the ability to compute the correct Reynolds stress anisotropy (for flows

Downloaded by [the LANL Research Library] at 12:39 21 December 2011

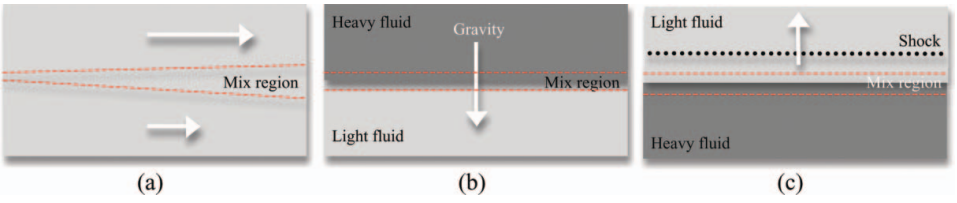

Figure 1. Schematics of (a) SD (plan view), (b) pressure-driven (Rayleigh–Taylor), and (c) shock-driven instabilities. The interfaces of these different density fluids form mixing regions when pressure and/or velocity gradients are present.

Downloaded by [the LANL Research Library] at 12:39 21 December 2011

which are clearly anisotropic) and they also had to vary the coefficients from flow to flow to achieve a good match. Stalsberg-Zarling and Gore [7] studied an extension to this model by including the transport equation for density-specific-volume covariance and a modified version of the turbulent viscosity hypothesis. Again, this model cannot capture the effects of Reynolds stress anisotropy in regions where velocity gradients are negligible.

Grègoire et al. [4] also presented a second-order turbulence model, very similar to the work of Besnard et al. [5]. Thus, they treat the fully compressible case, but they still make simplifying assumptions on the second moment, $\overline{\rho' v'}$, which are only valid in the Boussinesq limit. Their results compared well with shock tube data, e.g., the experimental work of Poggi et al. [8] and Andronov et al. [9]. Although Poggi et al. did measure second-moment statistics, Andronov et al. did not. Thus, the major comparison between the two experiments and the model was the mix width. Grègoire et al. did not extend their model to other classes of flows such as shear-driven (SD) or Rayleigh–Taylor (RT) mixing, primarily because DNS and experimental data were unavailable at that time.

Here, the fully compressible case is considered along with a transport equation for b, so that a no-mix or Boussinesq assumption is not necessary. In addition, to account for anisotropies in turbulent energy, we compute the components of the Reynolds stress using a transport equation. This also allows an anisotropic form of the turbulent diffusion terms to be included in constitutive models.

The purpose of this paper is twofold. First, we are interested in highlighting the importance of using the density-specific-volume covariance for a moment closure of VD turbulent flows, as opposed to the density variance, which is appropriate only in the Boussinesq limit. Second, we will apply a variable-density second-moment closure model, with the correct constitutive relations, to several different genres of flows, specifically, SD instability, Rayleigh–Taylor instability, and Richtmyer–Meshkov (RM) instability showing reasonable comparisons to DNS and experimental data. A schematic of these flows is shown in Figure 1 and the details of each flow are further discussed in §5.1, §5.2, §7.1, §7.2, and §7.3. These three classes of flows cover a wide range of applications where density fluctuations are expected to be important.

2. Governing equations

2.1 Instantaneous equations

The governing equations describing the flow of miscible mixtures of compressible materials are shown below [10, 11]

Downloaded by [the LANL Research Library] at 12:39 21 December 2011

Continuity:

$$\frac{\partial \rho}{\partial t} + (\rho u_j)_{,j} = 0. \tag{3}$$

Momentum:

$$\frac{\partial (\rho u_i)}{\partial t} + (\rho u_i u_j + P\delta_{ij})_{,j} = \tau_{ij,j} + \rho g_i. \tag{4}$$

Energy:

$$\frac{\partial}{\partial t}(\rho E) + (\rho u_j E + P u_j)_{,j} = \left(\tau_{ij} u_i - q_j^c - q_j^d\right)_{,j}. \tag{5}$$

Species Mass Fraction:

$$\frac{\partial (\rho c^n)}{\partial t} + \left(\rho c^n u_j\right)_{,j} = -j^n_{,j}, \tag{6}$$

where ρ is the material density, u is the fluid velocity, P is the pressure, τ is the molecular shear stress tensor, g is gravity, E is the total energy, q^c is the conductive heat flux, q^d is the interdiffusional enthalpy flux, c is the mass fraction of species n, and j is the diffusive mass fraction. The above equations should be supplemented with equations of state (pressure and caloric) and expressions for the molecular transport terms: viscous stresses, conduction, enthalpy diffusion, and mass diffusion.

2.2 Favre-averaged equations

Assuming a statistical description of turbulence, the governing equations are averaged over ensembles of independent realizations. The instantaneous variables in Equations (3)–(6) are decomposed into mean and deviation terms, such as $u_i = \bar{u}_i + u_i'$. Favre averages are then formed from the resultant terms, where $\tilde{u}_i = \bar{u}_i + \overline{\rho' u_i'}/\bar{\rho}$, $u_i'' = u_i' - \overline{\rho' u_i'}/\bar{\rho}$, and $\overline{\rho u''}_i = 0$. Neglecting the molecular transport terms, the averaged equations are:

Continuity:

$$\frac{\partial \bar{\rho}}{\partial t} + \left(\bar{\rho}\tilde{u}_j\right)_{,j} = 0. \tag{7}$$

Momentum:

$$\frac{\partial (\bar{\rho}\tilde{u}_i)}{\partial t} + \left(\bar{\rho}\tilde{u}_i\tilde{u}_j + \bar{P}\delta_{ij} + \bar{\rho}\tilde{R}_{ij}\right)_{,j} = \bar{\rho} g_i. \tag{8}$$

Energy:

$$\begin{aligned}\frac{\partial}{\partial t}\left(\bar{\rho}\tilde{E}\right) + \left(\bar{\rho}\tilde{u}_j\tilde{E}\right)_{,j} = &-(\bar{P}\tilde{u}_j)_{,j} - (\bar{\rho}\tilde{u}_i\tilde{R}_{ij})_{,j} - \left(\overline{P' u_j'}\right)_{,j} - \left(\overline{\rho I'' u_j''}\right)_{,j} \\ &- \frac{1}{2}\left(\overline{\rho u_i'' u_i'' u_j''}\right)_{,j} - \bar{q}^d_{j,j}.\end{aligned} \tag{9}$$

Species Mass Fraction:

$$\frac{\partial\left(\bar{\rho}\tilde{c}^{n}\right)}{\partial t}+\left(\bar{\rho}\tilde{u}_{j}\tilde{c}^{n}\right)_{,j}=-\left(\overline{\rho u_{j}^{\prime\prime}c^{\prime\prime n}}\right)_{,j} \tag{10}$$

where $\tilde{R}_{ij}$ is the Favre-averaged Reynolds stress ($\tilde{R}_{ij}=\overline{\rho u_{i}^{\prime\prime}u_{j}^{\prime\prime}}/\bar{\rho}$).

Similar to Reynolds averaging, the Favre average technique introduces additional unclosed terms, namely the Reynolds stress, the turbulent transport of the turbulent internal and kinetic energy, the turbulent flow work, and the turbulent transport of species n. A set of closure models is needed to complete the system of equations.

Downloaded by [the LANL Research Library] at 12:39 21 December 2011

3 Closure models

In this section, models are proposed to close the additional turbulence quantities shown in Equations (8)–(10). This involves modeling (a) the Reynolds stress, (b) turbulent contributions to the total energy, (c) interdiffusional enthalpy flux, and (d) the turbulent transport of species n. Ultimately, a set of constitutive relations and transport equations are sought to close the above equation set.

3.1 Reynolds stresses

Transport equations for the Reynolds stresses are derived from first principles. However, several models need to be incorporated to close the equation. The derivation of the Favre-averaged Reynolds stress transport equation can be found in [5, 12]. The exact equation is shown as follows:

$$\begin{aligned}\frac{\partial\left(\bar{\rho}\tilde{R}_{ij}\right)}{\partial t}+\frac{\partial}{\partial x_{k}}\left(\bar{\rho}\tilde{u}_{k}\tilde{R}_{ij}\right)=&\overbrace{a_{i}\frac{\partial\bar{P}}{\partial x_{j}}+a_{j}\frac{\partial\bar{P}}{\partial x_{i}}-\bar{\rho}\tilde{R}_{ik}\frac{\partial\tilde{u}_{j}}{\partial x_{k}}-\bar{\rho}\tilde{R}_{jk}\frac{\partial\tilde{u}_{i}}{\partial x_{k}}}^{\text{Production}}-a_{i}\frac{\partial\tilde{\tau}_{jk}}{\partial x_{k}}-a_{j}\frac{\partial\tilde{\tau}_{ik}}{\partial x_{k}}\\&\underbrace{-\frac{\partial}{\partial x_{k}}\overline{\rho u_{i}^{\prime\prime}u_{j}^{\prime\prime}u_{k}^{\prime\prime}}+\frac{\partial}{\partial x_{k}}\left(\overline{u_{i}^{\prime\prime}\tau_{jk}^{\prime\prime}}+\overline{u_{j}^{\prime\prime}\tau_{ik}^{\prime\prime}}\right)-\frac{\partial}{\partial x_{j}}\overline{u_{i}^{\prime\prime}P^{\prime}}-\frac{\partial}{\partial x_{i}}\overline{u_{j}^{\prime\prime}P^{\prime}}}_{\text{Transport}}\\&+\underbrace{\overline{P^{\prime}\frac{\partial u_{i}^{\prime\prime}}{\partial x_{j}}}+\overline{P^{\prime}\frac{\partial u_{j}^{\prime\prime}}{\partial x_{i}}}}_{\text{Pressure Strain}}-\underbrace{\overline{\tau_{jk}^{\prime\prime}\frac{\partial u_{i}^{\prime\prime}}{\partial x_{k}}}-\overline{\tau_{ik}^{\prime\prime}\frac{\partial u_{j}^{\prime\prime}}{\partial x_{k}}}}_{\text{Dissipation}}.\end{aligned} \tag{11}$$

The terms in the above equation are grouped into production, transport, pressure strain, and dissipation categories. The molecular shear terms are neglected and the remaining production terms are in closed form. The transport, pressure strain, and dissipation terms require models to close the above equation.

As a starting point, the transport terms are modeled as turbulent diffusion, using a formulation originally proposed by Daly and Harlow [13]. The pressure strain terms act to transfer energy between the components of the Reynolds stress tensor. These terms are traditionally modeled by a slow return to isotropy component and a rapid distortion component. Rotta [14] introduced a model for the slow return to isotropy, and Naot et al. [15] introduced the *isotropization of production* (IP) model for the rapid distortion effects.

This model was used by Launder et al. [16] and is traditionally referred to as the LRR-IP model.

The LRR-IP model for the pressure strain terms has been used since 1975 [16] and applied to a variety of engineering flows showing reasonable results and numerical stability with minimal computational power. Recently, several advanced models for the pressure strain terms have been investigated by Banerjee et al. [17], and the IP model (with the correct coefficients) produced reasonable results. Grègoire et al. [4] also used the IP model and showed good results in RM flows. Given the uncertainty of properly modeling the turbulent mass flux and its constitutive relations, the LRR-IP model was chosen as a starting place with the intent of eventually adopting more advanced models for the pressure strain terms.

The last term in the above equation denotes dissipation and represents the conversion of turbulent energy to heat. Ideally, this term should be modeled in an anisotropic form, but at high Reynolds numbers, where an inertial subrange exists, the dissipation is assumed to be isotropic. The buoyancy effects and anomalous anisotropy in the dissipation range [2, 3] will be addressed in a future work. Using these assumptions, the modeled form of the exact equation is then

$$\begin{aligned}\frac{\partial(\bar{\rho}\tilde{R}_{ij})}{\partial t} + (\bar{\rho}\tilde{u}_k\tilde{R}_{ij})_{,k} = {} & \overbrace{\left[a_i\bar{P}_{,j} + a_j\bar{P}_{,i}\right] - \bar{\rho}\left[\tilde{R}_{ik}\tilde{u}_{j,k} + \tilde{R}_{jk}\tilde{u}_{i,k}\right]}^{\text{Production}} \\ & + \underbrace{C_r\left(\frac{S}{\sqrt{K}}\bar{\rho}\tilde{R}_{kn}\tilde{R}_{ij,n}\right)_{,k}}_{\text{Diffusion}} - \underbrace{C_{r3}\bar{\rho}\frac{\sqrt{K}}{S}\left(\tilde{R}_{ij} - \frac{1}{3}\tilde{R}_{kk}\delta_{ij}\right)}_{\text{Return to Isotropy}} \\ & - \overbrace{C_{r1}\left[a_i\bar{P}_{,j} + a_j\bar{P}_{,i}\right] + C_{r2}\bar{\rho}\left[\tilde{R}_{ik}\tilde{u}_{j,k} + \tilde{R}_{jk}\tilde{u}_{i,k}\right]}^{\text{Rapid Distortion}} \\ & - \underbrace{C_{r2}\frac{2}{3}\bar{\rho}\tilde{R}_{mk}\tilde{u}_{m,k}\delta_{ij} + C_{r1}\frac{2}{3}a_k\bar{P}_{,k}\delta_{ij}}_{\text{Rapid Distortion}} - \underbrace{\bar{\rho}\frac{2}{3}\frac{K\sqrt{K}}{S}\delta_{ij}}_{\text{Dissipation}}, \end{aligned} \tag{12}$$

where K is the Favre-averaged turbulent kinetic energy ($K \equiv \tilde{R}_{ii}/2$), S is the turbulent length scale ($S \equiv K^{3/2}/\varepsilon$), and a_i is the mass-weighted turbulent velocity ($a_i \equiv -\overline{u_i''} = \overline{\rho' u_i'}/\bar{\rho}$). The first two terms on the right-hand side (RHS) are the production, and the remaining terms are models. It is noted that the model for the diffusion term is not the symmetric form, but this simplified model is applicable to 1-D-type flows.

In the equation above, closures are needed for the turbulent length scale (S) and the turbulent mass flux (ρa_i). These quantities are discussed below.

3.2 Length scale

Two equation models, such as the traditional k–ε model, have proven to be robust in a variety of flow regimes, which is an advantage over zero- or one-equation models. For high-Reynolds-number flows, this approach works well. However, as the turbulence becomes more anisotropic, two-equation models tend to fail [18]. In the present study, a turbulence length scale equation is preferred over a dissipation equation because physical intuition can be associated with it even at early times, when the dissipation may not be well defined

Downloaded by [the LANL Research Library] at 12:39 21 December 2011

in flows such as RT or RM instabilities. For instance, initializing a perturbation along an interface or knowing that turbulent eddies, generated by mixing binary fluids, cannot exceed the mix width are a few examples of physical intuition.

In order to obtain a transport equation for the turbulent length scale, first the turbulence energy equation is scaled using dimensional arguments [21] to obtain a dissipation equation of the form

$$\frac{\partial(\bar{\rho}\varepsilon)}{\partial t} + (\bar{\rho}\tilde{u}_j\varepsilon)_{,j} = -C_{\varepsilon 1}\frac{\varepsilon}{K}\bar{\rho}\tilde{R}_{ij}\tilde{u}_{i,j} + C_\varepsilon\left(\frac{K}{\varepsilon}\bar{\rho}\tilde{R}_{kn}\varepsilon_{,n}\right)_{,k} - C_{2\varepsilon}\bar{\rho}\frac{\varepsilon^2}{K} + C_{3\varepsilon}\frac{\varepsilon}{K}a_j\bar{P}_{,j}. \tag{13}$$

Several researchers [4, 5, 6, 19] have added an additional production term of the form $-C_{4\varepsilon}\bar{\rho}\varepsilon\bar{u}_{j,j}$ to potentially correct the behavior of the production term during compression and expansion [20]. However, they also set the coefficient to zero, which is justified for SD and RT flows, but the coefficient may require a non-zero value for RM flows (this is further discussed in §7.3). Using the definition of ε ($= K^{3/2}/\mathrm{S}$) and the turbulent kinetic energy equation (which is half the trace of Equation (12)), a transport equation for the turbulent length scale can be developed. The modeled form is shown as

$$\frac{\partial(\bar{\rho}S)}{\partial t} + \left(\bar{\rho}\tilde{u}_jS\right)_{,j} = \left(C_{\varepsilon 1}-\frac{3}{2}\right)\frac{S}{K}\bar{\rho}\tilde{R}_{ij}\tilde{u}_{i,j} + \left(C_{2\varepsilon}-\frac{3}{2}\right)\bar{\rho}K^{1/2} - \left(C_{3\varepsilon}-\frac{3}{2}\right)\frac{S}{K}a_j\bar{P}_{,j} + C_\varepsilon\frac{S^2}{K^{3/2}}\left(\frac{K}{S}\bar{\rho}\tilde{R}_{kn}S_{,n}\right)_{,k} + C_\varepsilon\frac{3}{2}\frac{S}{K}\bar{\rho}\tilde{R}_{kn}K_{,n}\left(\frac{S}{K^{1/2}}\right)_{,k}. \tag{14}$$

To simplify the model, it is assumed that the diffusion-like terms can be modeled as

$$C_\varepsilon\frac{S^2}{K^{3/2}}\left(\frac{K}{S}\bar{\rho}\tilde{R}_{kn}S_{,n}\right)_{,k} + C_\varepsilon\frac{3}{2}\frac{S}{K}\bar{\rho}\tilde{R}_{kn}K_{,n}\left(\frac{S}{K^{1/2}}\right)_{,k} \approx C_s\left(\frac{S}{\sqrt{K}}\bar{\rho}\tilde{R}_{kn}S_{,n}\right)_{,k}. \tag{15}$$

The modeled form of the turbulent length scale equation is then

$$\frac{\partial(\bar{\rho}S)}{\partial t} + \left(\bar{\rho}\tilde{u}_jS\right)_{,j} = \underbrace{-\frac{S}{K}\left(\frac{3}{2}-C_1\right)\bar{\rho}\tilde{R}_{ij}\tilde{u}_{i,j} + \frac{S}{K}\left(\frac{3}{2}-C_3\right)a_j\bar{P}_{,j} - \left(\frac{3}{2}-C_2\right)\bar{\rho}\sqrt{K}}_{\text{Net Production}} + \underbrace{C_s\left(\frac{S}{\sqrt{K}}\bar{\rho}\tilde{R}_{kn}S_{,n}\right)_{,k}}_{\text{Diffusion}}, \tag{16}$$

where C_s and $C_{1\ldots3}$ are coefficients. The terms on the RHS of the above equation are the net production and diffusion terms. The second term on the RHS of the above equation can be a production or destruction term, but it is typically described as the production one due to mixing of multiple materials in the absence of mean velocity gradients. The third term is derived from the dissipation term [21], but here it can be a production term if $C_2 > 3/2$.

Downloaded by [the LANL Research Library] at 12:39 21 December 2011

Downloaded by [the LANL Research Library] at 12:39 21 December 2011

3.3 Mass flux

The turbulent mass flux ($\bar{\rho}a_i$) is a result of Favre averaging. This term represents the coupling of the fluctuating density and velocity and is zero for incompressible, single-phase flows. It is the dominant form of advection in RT instabilities and also contributes to the production of the Reynolds stress in the presence of a pressure gradient. Simplifications to modeling this term have been studied by Dimonte and Tipton [22]. However, Livescu et al. [2] suggest that the rate of the turbulent mass flux is dependent on a delicate balance of large terms, implying that simple models may be calibrated for specific flows but the same calibration might not be valid for a wide variety of flows.

A general equation for the turbulent mass flux was derived from first principles by Besnard et al. [5] and the exact equation is shown as follows:

$$\frac{\partial\left(\bar{\rho}a_i\right)}{\partial t}+\left(\bar{\rho}\tilde{u}_k a_i\right)_{,k}=b(\bar{P}_{,i}-\bar{\tau}_{ki,k})-\tilde{R}_{ik}\bar{\rho}_{,k}+\bar{\rho}\left(a_k a_i\right)_{,k}-\bar{\rho}a_k\bar{u}_{i,k}-\bar{\rho}\left(\frac{\overline{\rho' u_i' u_k'}}{\bar{\rho}}\right)_{,k}+\bar{\rho}\overline{\upsilon'\left(P_{,i}'-\tau_{ki,k}'\right)}, \tag{17}$$

where b is the density-specific-volume covariance. The first two terms on the RHS are the production mechanisms. The third and fourth terms act like redistribution and/or advection (with the advection velocity equal to the mass flux) terms, while the fifth term is turbulence transport and the last term denotes destruction. To simplify the modeling approach, the molecular viscosity is neglected in the above equation.

The turbulence transport term is modeled using a gradient diffusion hypothesis

$$-\bar{\rho}\left(\frac{\overline{\rho' u_i' u_k'}}{\bar{\rho}}\right)_{,k}\approx\bar{\rho}C_a\left[\left(\frac{S}{\sqrt{K}}\tilde{R}_{kn}a_{i,n}\right)+\left(\frac{S}{\sqrt{K}}\tilde{R}_{in}a_{k,n}\right)\right]_{,k}. \tag{18}$$

For 1-D type simulations, the two terms can be combined. The last term is modeled as a simple decay of the form

$$\bar{\rho}\overline{\upsilon' P_{,i}'}\approx-C_{a1}\bar{\rho}\frac{\sqrt{K}}{S}a_i. \tag{19}$$

The above equation was suggested by Besnard et al. [5]. However, additional studies to improve this simple decay model and/or determine a transport equation for the left-hand side of Equation (19) are underway. Substituting equations (18) and (19) into Equation (17), a model for the turbulent mass flux is then obtained as follows:

$$\frac{\partial\left(\bar{\rho}a_i\right)}{\partial t}+\left(\bar{\rho}\tilde{u}_k a_i\right)_{k}=\underbrace{b\bar{P}_{,i}-\tilde{R}_{ik}\bar{\rho}_{,k}-\bar{\rho}a_k\bar{u}_{i,k}}_{\text{Net Production}}+\underbrace{\bar{\rho}\left(a_k a_i\right)_{,k}}_{\text{Redistribution}}+\underbrace{\bar{\rho}C_a\left(\frac{S}{\sqrt{K}}\tilde{R}_{kn}a_{i,n}\right)_{,k}}_{\text{Diffusion}}-\underbrace{C_{a1}\bar{\rho}\frac{\sqrt{K}}{S}a_i}_{\text{Destruction}}, \tag{20}$$

where a closure model is needed for b. The redistribution term serves to reallocate the turbulent mass flux across the mixing layer.

3.4 Density-specific-volume covariance

The density-specific-volume covariance, $b \equiv -\overline{\rho'(1/\rho)'}$, is a nonnegative measure of how well the instantaneous density and specific volume properties of the fluid agree (i.e., it can be shown that $b = \overline{\rho'^2/\bar{\rho}\rho}$, [5, 6]). If $b = 0$, the fluid is perfectly mixed. For completely segregated materials (e.g., the immiscible case) and binary systems, b has a simple formula: $b = \alpha_1\alpha_2(\rho_1 - \rho_2)^2/\rho_2\rho_1$ [6], where α_1 and α_2 are the volume fractions associated with the different fluid components in a binary system. As the density ratio in a binary system increases, b increases to infinity, while the normalized density variance remains bounded.

The role of $\overline{\upsilon'\rho'}$ is to moderate the turbulent mass flux production due to a pressure gradient [2]. In the Boussinesq limit (i.e., $A < 0.05$), the higher order terms in Equation (2) can be neglected, and the normalized density variance is applicable to low Atwood flows, where $\rho\prime << \bar{\rho}$ [5]. Models using the density variance rather than the density-specific-volume covariance are presented in [4]. Livescu et al. [2] compare the normalized density variance to the density-specific-volume covariance in a Rayleigh–Taylor (RT) simulation. They show that as the Atwood is raised, the density-specific-volume correlation is larger in magnitude than the normalized density variance on the heavy fluid (bubble) side and vice versa on the light fluid (spike) side. Thus, the energy conversion rate can be higher in the light fluid and lower in the heavy fluid when the higher order terms are neglected and the difference increases significantly with A [2]. This substantiates the need to model the density-specific-volume covariance as opposed to the density variance for large density differences leading to high Atwood numbers.

The transport equation for density-specific volume covariance was first derived by Besnard et al. [5], in the following form:

$$\frac{\partial b}{\partial t} + \bar{u}_k b_{,k} = -\frac{b+1}{\bar{\rho}}(\bar{\rho}a_k)_{,k} - \bar{\rho}\left(\overline{\upsilon' u_k'}\right)_{,k} - 2\bar{\rho}\left(\overline{\upsilon' d}\right), \tag{21}$$

where d is the dilatation ($= u'_{k,k}$) and υ' is the fluctuating specific volume. The transport term $(\overline{\upsilon' u_k'})$ is a second-order quantity and is unclosed. In order to close the equations, at the second level, we rewrite $(\overline{\upsilon' u_k'})$, by using the condition $\rho\upsilon = 1$ [2], and apply Reynolds decomposition to formulate

$$\overline{\upsilon' u_k'} = -\frac{\overline{\rho' u_k'}}{\bar{\rho}}\bar{\upsilon} - \frac{\overline{\rho'\upsilon' u_k'}}{\bar{\rho}}. \tag{22}$$

Modeling the triple correlation using a gradient diffusion hypothesis yields a practical form

$$\overline{\upsilon' u_k'} = -a_k\frac{b+1}{\bar{\rho}} - C_b\frac{S}{\sqrt{K}}\frac{\tilde{R}_{kn}}{\bar{\rho}}b_{,n}. \tag{23}$$

Downloaded by [the LANL Research Library] at 12:39 21 December 2011

By substituting Equation (23) into Equation (21) and multiplying by the mean density, a modeled form for b can be obtained

$$\frac{\partial(\bar{\rho}b)}{\partial t} + (\bar{\rho}b\tilde{u}_k)_{,k} = -2(b+1)a_k\bar{\rho}_{,k} + 2\bar{\rho}a_k b_{,k} + \bar{\rho}^2 C_b\left(\frac{S}{\bar{\rho}\sqrt{K}}\tilde{R}_{kn}b_{,n}\right)_{,k} - 2\bar{\rho}^2\varepsilon_b, \tag{24}$$

where $\varepsilon_b\left(=\overline{\upsilon' d}\right)$ is the dissipation of b. The first term on the RHS is the main production mechanism, followed by redistribution, diffusion, and destruction terms.

There are several models that could be used to determine ε_b. A rigorous form can be adopted where the transport equation for ε_b can be derived from the continuity equation. This method requires converting the density to specific volume, then multiplying by the dilatation, decomposing, and averaging. The general form of the transport equation for ε_b is then

$$\frac{\partial}{\partial t}(\bar{\rho}\varepsilon_b) + \left(\bar{\rho}\varepsilon_b\tilde{u}_j\right)_{,j} = \bar{\rho}\overline{\upsilon'\frac{\partial d}{\partial t}} + \bar{\rho}\bar{u}_j\overline{\upsilon' d}_{,j} - \bar{\rho}a_j\varepsilon_{b,j} + \bar{\rho}\varepsilon_b a_{j,j} + \bar{\rho}\varepsilon_b\tilde{u}_{j,j} - \bar{\rho}\bar{\upsilon}_{,j}\overline{u_j' d} - \bar{\rho}\overline{(\upsilon' u_j' d)}_{,j} + \bar{\rho}\overline{u_j'\upsilon' d}_{,j} + \bar{\rho}\bar{\upsilon}\overline{d^2} + 2\bar{\rho}\overline{\upsilon' d^2}. \tag{25}$$

The first two terms on the RHS of Equation (25) correspond to the material derivative of the dilatation and the fluctuating specific volume. An expression for these terms can be found by taking the divergence of the momentum equation and multiplying it by the fluctuating specific volume and then ensemble averaging. Although the above approach would be a more rigorous start for building a closure for ε_b, several complicated terms involving pressure fluctuation gradients coupled to specific volume gradients arise. The data necessary to pursue such a path are limited and will be discussed in a future work. For now, we will use a simple approach, by adopting the form of a decay model. Such a decay model was proposed by Besnard et al. [5], where ε_b is approximated as

$$\varepsilon_b \approx \frac{C_{b1}}{2}\frac{\sqrt{K}}{S}\frac{b}{\bar{\rho}}. \tag{26}$$

Substituting Equation (26) into Equation (24), the modeled equation for the density-specific-volume covariance is then

$$\frac{\partial(\bar{\rho}b)}{\partial t} + (\bar{\rho}b\tilde{u}_k)_{,k} = \underbrace{-2(b+1)a_k\bar{\rho}_{,k}}_{\text{Production}} + \underbrace{2\bar{\rho}a_k b_{,k}}_{\text{Redistribution}} + \underbrace{\bar{\rho}^2 C_b\left(\frac{S}{\bar{\rho}\sqrt{K}}\tilde{R}_{mn}b_{,n}\right)_{,m}}_{\text{Diffusion}} - \underbrace{C_{b1}\bar{\rho}\frac{\sqrt{K}}{S}b}_{\text{Destruction}}. \tag{27}$$

Equations (16), (20), and (27) supply the necessary closure to the VD Reynolds stress model (Equation (12)).

Downloaded by [the LANL Research Library] at 12:39 21 December 2011

3.5 Total specific energy

In the total energy equation (9), the turbulent transport terms are modeled using the gradient diffusion hypothesis

$$-(\overline{P'u'_j})_{,j} - (\overline{\rho I'' u''_j})_{,j} - \frac{1}{2}\left(\overline{\rho u''_i u''_i u''_j}\right)_{,j} \approx \left(\bar{\rho}\tilde{R}_{ij}\frac{S}{\sqrt{K}}[C_k K_{,j} + C_e k_{eff}\tilde{T}_{,j}]\right)_{,i}, \tag{28}$$

where the pressure flow work term is neglected when compared to the other terms and the turbulent transport of internal energy is modeled in the form of turbulent conduction. The exact terms can also be modeled using the turbulent viscosity ($\nu_t = C_{\mu s} S\sqrt{K}$) concept. The interdiffusional enthalpy flux ($\bar{q}_j^d$) was also incorporated based on the work of Cook [11]. The total energy equation is then shown as

$$\frac{\partial}{\partial t}(\bar{\rho}\tilde{E}) + (\bar{\rho}\tilde{u}_j\tilde{E})_{,j} = -(\bar{P}\bar{u}_j)_{,j} - (\tilde{u}_i\bar{\rho}\tilde{R}_{ij})_{,j} + \left(\bar{\rho}\tilde{R}_{ij}\frac{S}{\sqrt{K}}\left[C_k K_{,j} + C_e\frac{C_v}{\mathrm{Pr}_t}\tilde{T}_{,j} + C_c\bar{h}^n\tilde{c}^n_{,j}\right]\right)_{,i} \tag{29a}$$

or using the turbulent viscosity

$$\frac{\partial}{\partial t}(\bar{\rho}\tilde{E}) + (\bar{\rho}\tilde{u}_j\tilde{E})_{,j} = -(\bar{P}\bar{u}_j)_{,j} - (\tilde{u}_i\bar{\rho}\tilde{R}_{ij})_{,j} + \left(\bar{\rho}\nu_t\left[K_{,j} + \frac{C_v}{\mathrm{Pr}_t}\tilde{T}_{,j} + \frac{1}{\sigma_c}\bar{h}^n\tilde{c}^n_{,j}\right]\right)_{,i}, \tag{29b}$$

where $C = 3C_\mu/2\sigma$, $\sigma_c = 0.75$, h is the enthalpy, and the turbulent Prandtl number is defined as $Pr_t = C_v\nu_t/k_{\mathrm{eff}}$. The average internal energy is $\tilde{I} = \tilde{E} - \frac{1}{2}\bar{\rho}\tilde{u}_i\tilde{u}_i - K$; the average temperature is determined from the caloric equation of state $\tilde{I} = C_v\tilde{T}$, and the average pressure of the gaseous mixture is modeled by the ideal-gas equation of state

$$\bar{P} = (1-\gamma)\,\bar{\rho}\tilde{I}, \tag{30}$$

where γ is the ratio of specific heats.

3.6 Species mass fractions

In the species mass fraction equation (10), the turbulent transport terms are modeled using the gradient diffusion hypothesis, such as

$$-\left(\overline{\rho u''_j c''^n}\right)_{,j} \approx \left(C_c\frac{S}{\sqrt{K}}\bar{\rho}\tilde{R}_{jm}\tilde{c}^n_{,m}\right)_{,j} = J^n_{j,j}, \tag{31}$$

where $\tilde{c}^n_{,m}$ is the mean concentration gradient of the species n. The modeled mass fraction transport equation then becomes

$$\frac{\partial(\bar{\rho}\tilde{c}^n)}{\partial t} + (\bar{\rho}\tilde{u}_j\tilde{c}^n)_{,j} = J^n_{j,j}. \tag{32}$$

Downloaded by [the LANL Research Library] at 12:39 21 December 2011

4. VD turbulence equations

In summary, the model consists of the Favre-averaged VD continuity, momentum, energy, and mass fraction equations ((7), (8), (29), (32)), supplemented with equations for second-order quantities, such as the Reynolds stress, turbulence length scale, mass flux, and density-specific-volume correlation ((12), (16), (20), (27)) and equations of state for the internal energy and pressure. This closes the system of equations. The exact and modeled forms of the equations are shown in Appendixes A.1 and A.2 for convenience.

5. Model calibration

The models for VD turbulence contain several coefficients that need calibration. The ideal method to calibrate these coefficients is to simplify the flow in various configurations, such that most of the terms are zero and the remaining nonzero terms are different for each of the configurations considered. In previous studies of single-phase, Boussinesq flows, the first flow used in calibration of moment closures is the isotropic, homogeneous turbulence decay. Under these conditions, the gradients of mean quantities are zero, leaving a time rate of change balanced by the decay rate. This allows calibration of the decay coefficient and is the method used to determine the dissipation coefficient in the dissipation or turbulence length scale equation. Similarly, the production and diffusion coefficients are also found from simple flows. For instance, in wall flows, the coefficients in the dissipation equation are related, and a simple expression can be developed to determine the value of the diffusion coefficient based on the value of the remaining coefficients [23].

Similar ideas can be used to determine the coefficients for the set of VD equations. Ideally, data from the isotropic, homogeneous decay of a fluid mixture can be used to determine the coefficients of the destruction terms in the turbulent mass flux and the density-specific-volume covariance equations. These data would also show if the single-phase destruction coefficient for the turbulent length scale is valid for the destruction of turbulence energy in the mix region of VD flows. However, such fundamental experimental data for this type of flow are unavailable. Therefore, an interim solution is to reduce the VD equations to single-phase and apply the known coefficients where necessary. The remaining coefficients can be calibrated by applying the VD equations to instabilities that promote mixing, such as shear-driven (Kelvin–Helmholtz or in short KH) and pressure-driven (Rayleigh–Taylor) instabilities. These canonical instabilities allow calibration of the remaining model coefficients.

5.1 SD instability

An SD instability arises at the interface between two bulk stream fluids having different mean velocities, shown in Figure 1(a). Under certain conditions, the instability along the interface curls the initially parallel streams into vortical structures, which grow and entrain more pure fluid on either side of the interface, all the while becoming increasingly more effective at small-scale mixing. For low Mach number and constant density fluids, the turbulent mass flux and the density-specific-volume covariance are negligible. For this case, the Reynolds stress and the turbulent length scale equations are reduced to

Reynolds Stress:

$$\frac{\partial \tilde{R}_{11}}{\partial t} + (\tilde{u}_k \tilde{R}_{11})_{,k} = 2\,(C_{r2} - 1)\,\tilde{R}_{1k}\tilde{u}_{1,k} - C_{r2}\frac{2}{3}\tilde{R}_{mk}\tilde{u}_{m,k} + C_r\left(\frac{S}{\sqrt{K}}\tilde{R}_{km}\tilde{R}_{11,m}\right)_{,k} - C_{r3}\frac{\sqrt{K}}{S}(\tilde{R}_{11}) + \frac{2}{3}\,(C_{r3} - 1)\,\frac{K\sqrt{K}}{S}, \tag{33}$$

Downloaded by [the LANL Research Library] at 12:39 21 December 2011

$$\frac{\partial \tilde{R}_{22}}{\partial t} + (\tilde{u}_k \tilde{R}_{22})_{,k} = 2\,(C_{r2} - 1)\,\tilde{R}_{2k}\tilde{u}_{2,k} - C_{r2}\frac{2}{3}\tilde{R}_{mk}\tilde{u}_{m,k} + C_r\left(\frac{S}{\sqrt{K}}\tilde{R}_{km}\tilde{R}_{22,m}\right)_{,k} - C_{r3}\frac{\sqrt{K}}{S}\tilde{R}_{22} + \frac{2}{3}\,(C_{r3} - 1)\,\frac{K\sqrt{K}}{S}, \tag{34}$$

$$\frac{\partial \tilde{R}_{12}}{\partial t} + (\tilde{u}_k \tilde{R}_{12})_{,k} = (C_{r2} - 1)\,(\tilde{R}_{1k}\tilde{u}_{2,k} + \tilde{R}_{2k}\tilde{u}_{1,k}) + C_r\frac{\partial}{\partial x_k}\left(\frac{S}{\sqrt{K}}\tilde{R}_{km}\frac{\partial \tilde{R}_{12}}{\partial x_m}\right) - C_{r3}\frac{\sqrt{K}}{S}\tilde{R}_{12}. \tag{35}$$

Turbulent length scale:

$$\frac{\partial S}{\partial t} + (\tilde{u}_j S)_{,j} = -\frac{S}{K}\left(\frac{3}{2} - C_1\right)\tilde{R}_{ij}\tilde{u}_{i,j} - \left(\frac{3}{2} - C_2\right)\sqrt{K} + C_s\left(\frac{S}{\sqrt{K}}\tilde{R}_{mn}S_{,n}\right)_{,m}. \tag{36}$$

The coefficients that will be calibrated based on the shear-driven instability data are C_{r2}, C_{r3}, C_r, C_1, C_2, and C_s. The experimental data of Bell and Mehta [24], who studied a spatially growing layer, and the DNS of Rogers and Moser [25], who studied a temporally growing layer, are mainly used for this calibration. The mixing thickness Reynolds numbers were ~30,600 and ~20,000 [25], respectively. In this study, the model was set up as a temporally growing layer.

For single-phase turbulence, the coefficient $C_{r2} = 0.6$ agrees with rapid distortion theory [21]. The coefficient C_2 (= 1.92) is found from isotropic homogeneous turbulence decay. The coefficient associated with the slow return to isotropy, C_{r3} (= 1.8), is given by Launder [26].

As a starting point, the diffusion coefficients C_r and C_s will be estimated based on the studies of Livescu et al. [2] and Banerjee et al. [27]. They showed that the turbulent viscosity coefficient C_μ should be 0.28 in the RT mixing layer rather than 0.09, which is found from shear layers. The DNS results of Ristorcelli and Clark [28] showed that the turbulent length scale (S) is fairly constant across the low Atwood number RT mix. Using the data from [28], Banerjee et al. [6] found that σ_s should be approximately 0.1 to obtain a flat profile for the turbulent length scale. The formulation $C = 3C_\mu\,/2\sigma$ can be used to extend the value of the diffusion coefficient based on isotropic turbulent viscosity to anisotropic diffusion [4]; in this case, $C_r = 0.42$ and $C_s = 4.2$. Although these coefficients were used as a starting point, it was found that the self-similar dimensionless mix width visually agreed with the experimental data [24] and DNS [25]. In addition, Banerjee et al. [6] showed that the isotropic turbulent viscosity diffusion models for turbulent energy also matched the data of Bell and Mehta [24].

The coefficient $C_1 = 1.44$ has been applied to a wide set of data ranging from single-phase highly curved duct flows [18] to particle-laden channel flows [29], both of which used the dissipation equation. It is a standard constant that is used in many computational fluid dynamics (CFD) packages and applied to many engineering phenomena. However, a comparison of the second-moment model using $C_1 = 1.44$ to experimental and DNS data is shown in Figure 2. In this figure, all three Reynolds stress components underpredict the dimensionless magnitude of the data. Since the coefficients for rapid distortion are fixed ($C_{r2} = 0.6$, [21]), the remaining coefficient that can affect the magnitudes of the Reynolds

Downloaded by [the LANL Research Library] at 12:39 21 December 2011

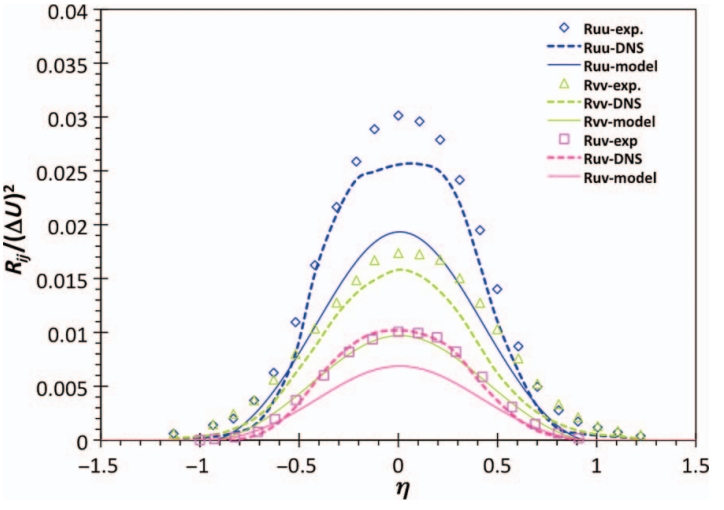

Figure 2. Comparison of a second-moment closure prediction with DNS results (Rogers and Moser [25]) and experimental data (Bell and Mehta [24]) with $C_1 = 1.44$, $\eta = (y - y_{c1})/\delta$, where y_{c1} is the value at the centerline of the mixing layer.

stress is C_1, which is related to the self-similar growth rate of a shear layer. The self-similar growth rate (β) of a temporal SD mixing layer is given by [21]

$$\beta \approx \frac{1}{U_s}\frac{d\delta}{dt}, \tag{37}$$

where U_s is the characteristic velocity and δ is the mixing layer width. The model prediction of the growth rate is improved by lowering the coefficient C_1. The predicted growth rate is 0.065 (0.045) for $C_1 = 1.2$ (1.44), respectively. The lower value of C_1 provides growth rates that are closer to those reported by various authors: 0.069 [21], 0.076 [24]. To account for these considerations, $C_1 = 1.2$ is used in the present model.

The coefficients for a second-moment closure applied to single-phase, single-component SD instabilities are provided in Table 1. The traditional coefficients used in the dissipation equation are also provided in Table 1 for comparison.

5.2 Buoyancy or pressure-driven instability

Buoyancy or pressure-driven instabilities arise when two fluids with different densities share a common interface in the presence of acceleration, shown in Figure 1(b). The acceleration is usually associated with a body force, such as gravity. A canonical example

Table 1. Coefficients for single-phase, single-component flows.

	C_{r2}	C_{r3}	C_r	C_s	C_1	C_2
ε-eqn.	0.6	1.8	0.22	0.15	1.44	1.92
S-eqn.	0.6	1.8	0.42	4.2	1.2	1.92

Downloaded by [the LANL Research Library] at 12:39 21 December 2011

is the RT instability in which a heavy fluid is set above a lighter fluid. The heavy fluid penetrates (spikes) and lighter fluid rises (bubbles) creating a mixing zone. In the classical RT instability, the flow is homogeneous in the horizontal directions, so that the governing equations can be plane-averaged and the turbulence quantities become one-dimensional. The equations, simplified for this flow, are shown below

Reynolds Stress:

$$\frac{\partial(\bar{\rho}\tilde{R}_{22})}{\partial t} + (\bar{\rho}a_3\tilde{R}_{22})_{,3} = C_r\left(\frac{S}{\sqrt{K}}\bar{\rho}\tilde{R}_{kn}\tilde{R}_{22,n}\right)_{,k} - C_{r3}\bar{\rho}\frac{\sqrt{K}}{S}\left(\tilde{R}_{22} - \frac{1}{3}\tilde{R}_{kk}\right) - C_{r2}\frac{2}{3}\bar{\rho}\tilde{R}_{33}a_{3,3} + C_{r1}\frac{2}{3}a_3\bar{P}_{,3} - \bar{\rho}\frac{2}{3}\frac{K\sqrt{K}}{S}, \tag{38}$$

$$\frac{\partial(\bar{\rho}\tilde{R}_{33})}{\partial t} + (\bar{\rho}a_3\tilde{R}_{33})_{,3} = 2(1 - C_{r1})a_3\bar{P}_{,3} + 2\bar{\rho}(C_{r2} - 1)\tilde{R}_{33}a_{3,3} + C_r\left(\frac{S}{\sqrt{K}}\bar{\rho}\tilde{R}_{kn}\tilde{R}_{33,n}\right)_{,k} - C_{r3}\bar{\rho}\frac{\sqrt{K}}{S}\left(\tilde{R}_{33} - \frac{1}{3}\tilde{R}_{kk}\right) - C_{r2}\frac{2}{3}\bar{\rho}\tilde{R}_{33}a_{3,3} + C_{r1}\frac{2}{3}a_3\bar{P}_{,3} - \bar{\rho}\frac{2}{3}\frac{K\sqrt{K}}{S}. \tag{39}$$

Turbulent mass flux:

$$\frac{\partial(\bar{\rho}a_3)}{\partial t} = b\bar{P}_{,3} - (\tilde{R}_{33} + a_3a_3)\bar{\rho}_{,3} + \bar{\rho}C_a\left(\frac{S}{\sqrt{K}}\tilde{R}_{kn}a_{3,n}\right)_{,k} - C_{a1}\bar{\rho}a_3\frac{\sqrt{K}}{S}. \tag{40}$$

Density-specific-volume covariance:

$$\frac{\partial(\bar{\rho}b)}{\partial t} + (\bar{\rho}a_3b)_{,3} = 2\bar{\rho}a_3b_{,3} - 2(b+1)a_3\bar{\rho}_{,3} + \bar{\rho}^2C_b\left(\frac{S}{\bar{\rho}\sqrt{K}}\tilde{R}_{kn}b_{,n}\right)_{,k} - C_{b1}\bar{\rho}\frac{\sqrt{K}}{S}b. \tag{41}$$

Turbulence length scale:

$$\frac{\partial(\bar{\rho}S)}{\partial t} + (\bar{\rho}a_3S)_{,3} = -\frac{S}{K}\left(\frac{3}{2} - C_1\right)\bar{\rho}\tilde{R}_{33}a_{3,3} - \left(\frac{3}{2} - C_2\right)\bar{\rho}\sqrt{K} + C_s\left(\frac{S}{\sqrt{K}}\bar{\rho}\tilde{R}_{kn}S_{,n}\right)_{,k} + \frac{S}{K}\left(\frac{3}{2} - C_3\right)a_3\bar{P}_{,3}. \tag{42}$$

Species Concentration:

$$\frac{\partial(\bar{\rho}\tilde{c}^n)}{\partial t} + (\bar{\rho}a_3\tilde{c}^n)_{,3} = \left(C_c\frac{S}{\sqrt{K}}\bar{\rho}\tilde{R}_{33}\tilde{c}^n_{,3}\right)_{,3}. \tag{43}$$

The coefficients that will be calibrated based on the RT instability data are C_{r1}, C_a, C_{a1}, C_b, C_{b1}, C_3, and C_c. Two datasets from some of the largest RT simulations to date are mainly used for this calibration. First is at $A = 0.04$, from Livescu et al. [3], and second is

Downloaded by [the LANL Research Library] at 12:39 21 December 2011

the $A = 0.5$ simulation of Cabot and Cook [30] as analyzed by Livescu et al. [2]. The two datasets report bulk Reynolds numbers of 35,000 and 32,000 based on the visual thickness, respectively, and they are denoted hereafter as RT1 and RT2.

5.2.1 *Calibrating the coefficient for the destruction term within the turbulent mass flux equation*

The RT1 and RT2 datasets provide information to calibrate the coefficient C_{a1}. The coefficient C_{a1} can be found by setting the exact destruction term to the modeled form. The coefficient should then behave as

$$C_{a1} \approx -\overline{\upsilon' \left(\frac{\partial P'}{\partial x_i} \right)} \frac{S}{a_i \sqrt{K}}. \tag{44}$$

Ruffin et al. [31] and Chassaing [32] suggested $C_{a1} = 3.0$, 5.3 respectively. Here, we calibrate the value of C_{a1} using the RT1 [3] and RT2 [30, 2] datasets described above. Figure 3 shows the coefficient C_{a1} across the dimensionless mix zone for the two Atwood numbers. Although a typical decay model for a_i may not be appropriate to close the destruction term, due to the complexities of modeling the specific volume pressure gradient correlation, $\bar{\rho}\overline{\upsilon' P'_{,i}}$, the simple decay model was adopted here, as a starting point. Thus, C_{a1} is taken as 3.2, which was determined by averaging over a portion of the mixing layer. Further extensions of this model will be presented in future work.

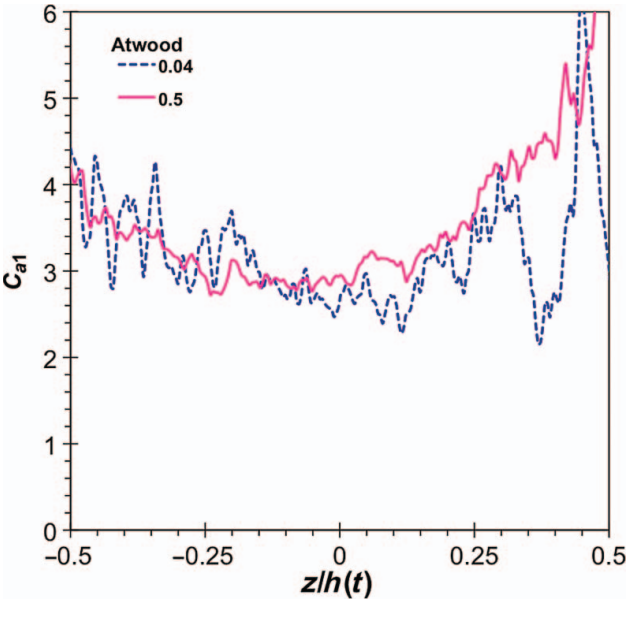

Figure 3. The variation of C_{a1} across the mixing layer of a Rayleigh–Taylor instability. The self-similar DNS data at $A = 0.04$ (Livescu et al. [3]) and $A = 0.5$ (Cabot and Cook [30], Livescu et al. [2]) were used to determine C_{a1} from Equation (44).

Downloaded by [the LANL Research Library] at 12:39 21 December 2011

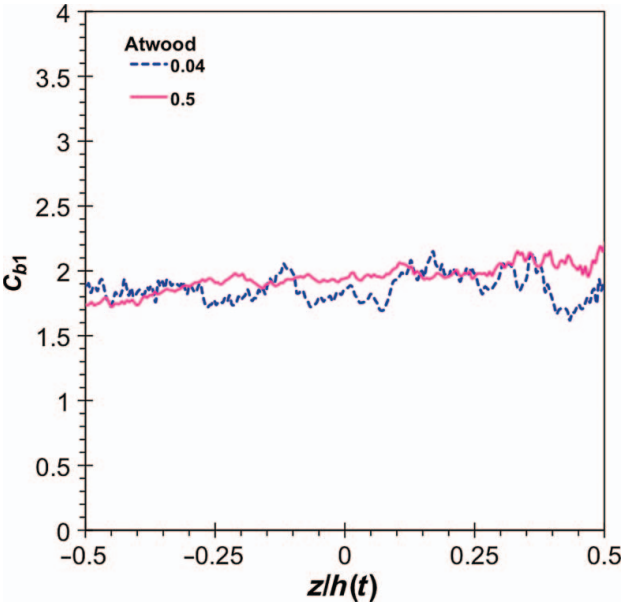

Figure 4. The variation of C_{b1} across the mixing layer of a Rayleigh–Taylor instability. The self-similar DNS data at $A = 0.04$ (Livescu et al. [3]) and $A = 0.5$ (Cabot and Cook [2], Livescu et al. [3]) were used to determine C_{b1} from Equation (45).

5.2.2 *Calibrating the coefficient for the destruction term within the density-specific-volume covariance equation*

RT1 and RT2 datasets also provide information to calibrate the coefficient C_{b1}. The method of determining C_{b1} is similar to the method for determining C_{a1}. By setting the modeled form of the destruction term equal to the actual destruction term, C_{b1} can be obtained

$$C_{b1} \approx 2\bar{\rho}\overline{v'd}\frac{S}{b\sqrt{K}}. \tag{45}$$

Figure 4 shows the value of C_{b1} for RT1 and RT2. The value is reasonably constant across the layer and a value of 2.0 was chosen to be consistent with the production terms in Equation (27). This suggests that the turbulence and mixing time scales are nearly equal when the flow is self-similar [28].

5.2.3 *Calibrating growth rates and diffusion coefficients*

The dimensionless growth rate (α) of the mixing layer can be computed from a quadratic formulation for the mix width, $h(t)$, derived by Ristorcelli and Clark [28]. An equivalent formula, which avoids the time derivative, is given in [3]

$$\alpha = \left(\frac{h(t)^{1/2} - h(t_0)^{1/2}}{(Ag)^{1/2}(t - t_0)}\right)^2, \tag{46}$$

Downloaded by [the LANL Research Library] at 12:39 21 December 2011

Table 2. Coefficients for single-phase, single and multicomponent flows

	C_{r1}	C_{r2}	C_{r3}	C_r	C_a	C_{a1}	C_b	C_{b1}	C_c	C_s	C_1	C_2	C_3	C_μ
ε-eqn.	0.3	0.6	1.8	0.22	0.18	3.0	0.18	3.0	0.18	0.15	1.44	1.92	0.95	0.09
S-eqn.	0.3	0.6	1.8	0.42	0.3	3.2	0.3	2.0	0.56	4.2	1.2	1.92	1.2	0.28

The coefficients for ε-eqn. are given in [4].

where, t_0 is an arbitrary time in the self-similar regime. The formulation used to compute the total mixing layer width, $h(t)$, is that of Andrews and Spalding [33] defined as

$$h(t) = 6\int_{-\infty}^{\infty} f_v\,(1 - f_v)\,dz, \quad \text{where} \quad f_v = \frac{\rho_{mix} - \rho_{\min}}{\rho_{\max} - \rho_{\min}}, \tag{47}$$

and where the factor of six derives from considering the width of a linear profile. Coefficients C_3, C_a, and C_b were set to match the dimensionless growth rates and the dimensionless mixing layer width. At $A = 0.04$, the α produced by the model is 0.041, compared to 0.0412 found from RT1. At $A = 0.5$, the α given by the model is 0.046, compared to 0.0416 found from RT2. Both of these comparisons were made with C_3 set to 1.2. The coefficients C_a and C_b were set to 0.3 to match the nondimensional width between the experimental [27] and DNS data. The value for C_c was chosen based on the relationship $C_c = (3/2)\,C_{\mu s}/\sigma_c$ where $C_{\mu s} = 0.28$ and a turbulent Schmidt number taken as $\sigma_c = 0.75$, suggested by [4]. The coefficient C_{r1} was taken as 0.3, also suggested in Ref. [4] and further discussed in §7.2.2.

5.3 Model coefficients

Based on the above methods, the model coefficients were found from DNS and experimental data for SD and RT instabilities. A list of coefficients are shown in Table 2 along with the coefficients used by Grègoire et al. [4], which used a dissipation equation and is shown for comparison. Overall, it was found that C_3 is the major contributor to the RT mixing layer growth, whereas C_1 is the major contributor to the shear-driven mixing layer growth. The remaining differences are in the diffusion terms and are primarily due to the different definitions of the turbulence time scale.

6. Numerical method

The Reynolds stress model was implemented into a compressible 3D Eulerian hydrocode [34]. The code uses a Godunov scheme to solve the mass, momentum, and energy equations while equations for the turbulence and mix quantities are solved using traditional finite-volume methods. Adaptive Mesh Refinement (AMR) is also used near the interfaces of materials or shocks, where density, pressure, and velocity gradients are the basic criteria for mesh refinement (additional information on AMR can be found in [34] and [35]). The boundary conditions are reflective or symmetric and the domain was sized such that the flow did not reach the boundaries.

To ensure that the solution is independent of the mesh, a grid resolution study was performed. For self-similar flows, the run time was extended to ensure that a self-similar state was achieved; e.g., in SD flows, $\mathrm{d}(R_{11}/(\Delta U)^2)/\mathrm{d}t \sim 0$, and in RT mixing, $\mathrm{d}b/\mathrm{d}t \sim 0$, and that the growth parameter α (based on the total mixing layer width) reaches a self-similar value [30]. For the RM simulation, the local mesh size ($\sim$78 μm) was decreased by a factor of 2 until the axial Reynolds stress component was found to be visually similar ($\sim$ 9 μm).

Downloaded by [the LANL Research Library] at 12:39 21 December 2011

The number of grid points used in each simulation were 8000, 13,024, and 5118, and time steps were on the order of 10^{-8}, 10^{-6}, and 10^{-8} for SD, RT, and RM flows, respectively. All runs were completed in less than 24 hours on eight CPUs.

6.1 Initialization

For gravity-induced turbulence (RT), the turbulent kinetic energy and turbulence length scale were initialized with small but nonzero values that were constant across the domain. The turbulent kinetic energy was then evenly distributed across the diagonal components of the Reynolds stress tensor while the off-diagonal components were initialized to zero.

For shear- and shock-induced turbulence (KH & RM), the turbulent kinetic energy was initialized as $K_o = \zeta\,(\Delta U)^2$, where ζ is the turbulence intensity (assumed to be $\sim$1%) and ΔU is the change in velocity across the interface. The jump conditions were set up at the interface of the materials or regions. The turbulent kinetic energy was then isotropically distributed across the diagonal components of the Reynolds stress tensor, while the off-diagonal components were initialized to zero. The turbulent length scale was initialized based on the perturbation scales at the interface. The turbulent mass flux was initialized as zero across the domain and the density-specific-volume covariance was initialized as the two-fluid value at the interface of the fluids; additional studies on initialization are currently underway. Since the code is compressible, the temperature was increased in the RT simulation to suppress shock formations.

7. Results

In order to validate the capability of the model, it is applied to three sets of instabilities that create a turbulent mixing zone (TMZ). First is a temporal SD mixing layer, where the model is compared to DNS [25] and experimental data [24]. Second is an RT mixing layer that is driven by an initial discontinuity in the pressure gradient at the interface between two fluids with different densities. The test data are the two DNS datasets, RT1 and RT2 described above, along with the experimental data of Banerjee et al. [27]. Finally, the model is applied to the RM instability, where a shock is passed through an interface between different density fluids. For this case, the model is compared with the measurements of turbulence quantities in a shock tube, provided by Poggi et al. [8].

7.1 SD instability

The experimental dataset of Bell and Mehta [24] and the DNS of Rogers and Moser [25], both addressing the constant density case, are used to test the model which was set up as a temporally growing mixing layer. The Reynolds stress data are nondimensionalized by the square of the velocity difference and compared in Figure 5(a).

Overall, the second-moment closure is in reasonable agreement with the two datasets. However, it is noticed that the model does not accurately predict the magnitude of R_{22}, and although not shown, the model predicts that $R_{22} = R_{33}$, which is contrary to both datasets. This may be a weakness in the models that were chosen to represent the pressure strain terms and the turbulence length scale, the latter of which is assumed to be isotropic.

The mean velocity profile, shown in Figure 5(b), compares well with the error function theory (described in [21, 24]) and both the experimental data and DNS in the self-similar regime.

Downloaded by [the LANL Research Library] at 12:39 21 December 2011

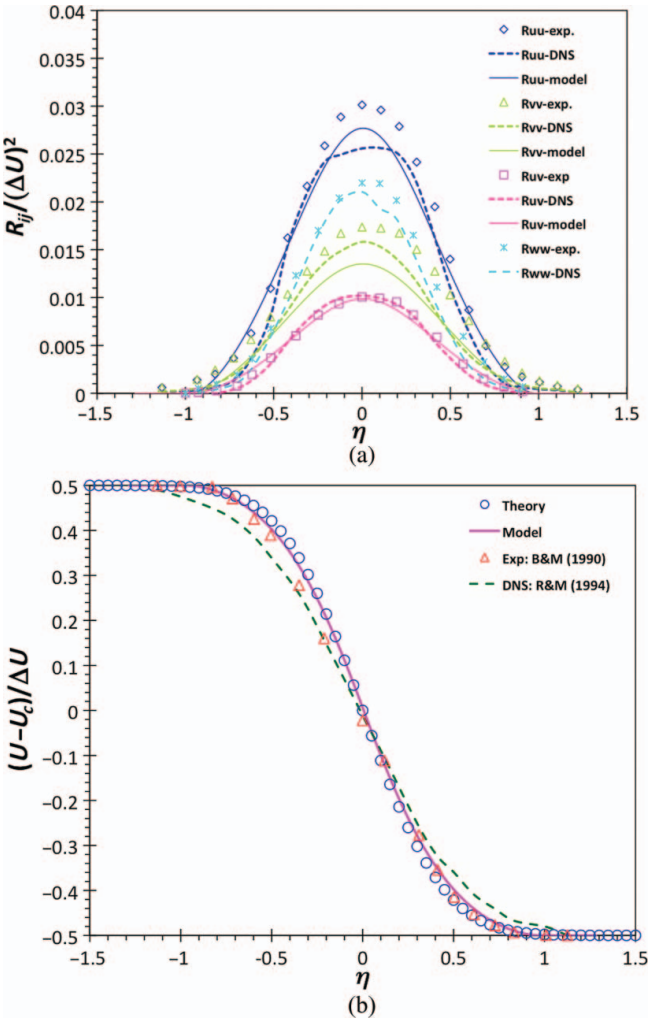

Figure 5. Comparison of a second-moment closure with DNS results (Rogers and Moser [25]) and experimental data (Bell and Mehta [24]); (a) Reynolds stress components and (b) velocity profile comparisons are made with $C_1 = 1.2$, see Figure 2 caption for the definition of η.

7.2 RT instability

RT instabilities arise when an external acceleration is applied in the direction of a dense fluid over a light fluid (shown in Figure 1(b)). In RT flows, the main production mechanisms are the pressure gradient coupled to the density-specific-volume covariance and the Reynolds stress coupled to the density–velocity covariance.

7.2.1 Nondimensionalization procedure

The Rayleigh–Taylor (RT) Direct Numerical Simulation (DNS) results of Cabot and Cook [30] analyzed by Livescu et al. [2] at moderate Atwood and Livescu et al. [3] at low Atwood numbers (0.5 and 0.04, respectively) were used to evaluate the coefficients and tune

Downloaded by [the LANL Research Library] at 12:39 21 December 2011

the Favre-averaged model. In order to compare the model with the DNS and experimental results, the following nondimensionalization procedure was taken to account for the differences in length and time scales. The length scales were nondimensionalized by the mixing layer width, $h(t)$ – the total width, determined by Equation (47). The time scales were nondimensionalized by

$$\tau = \left(\frac{h(t)}{A\,|g|}\right)^{1/2} = \sqrt{\alpha}t, \tag{48}$$

where α is the dimensionless growth rate of the mix layer in the self-similar regime. This nondimensionalization procedure collapses the RT DNS once a self-similar state has been reached. Here, the velocity scale is defined as: $\lambda = h(t)/\sqrt{\alpha}t = \dot{h}/2\sqrt{\alpha}$ and $\lambda^2 = \dot{h}^2/4\alpha$ [28]. Using this technique, the turbulent kinetic energy and turbulent mass flux can be collapsed and shown to be independent of temporal and spatial growth, as shown in Figure 6 for DNS.

Downloaded by [the LANL Research Library] at 12:39 21 December 2011

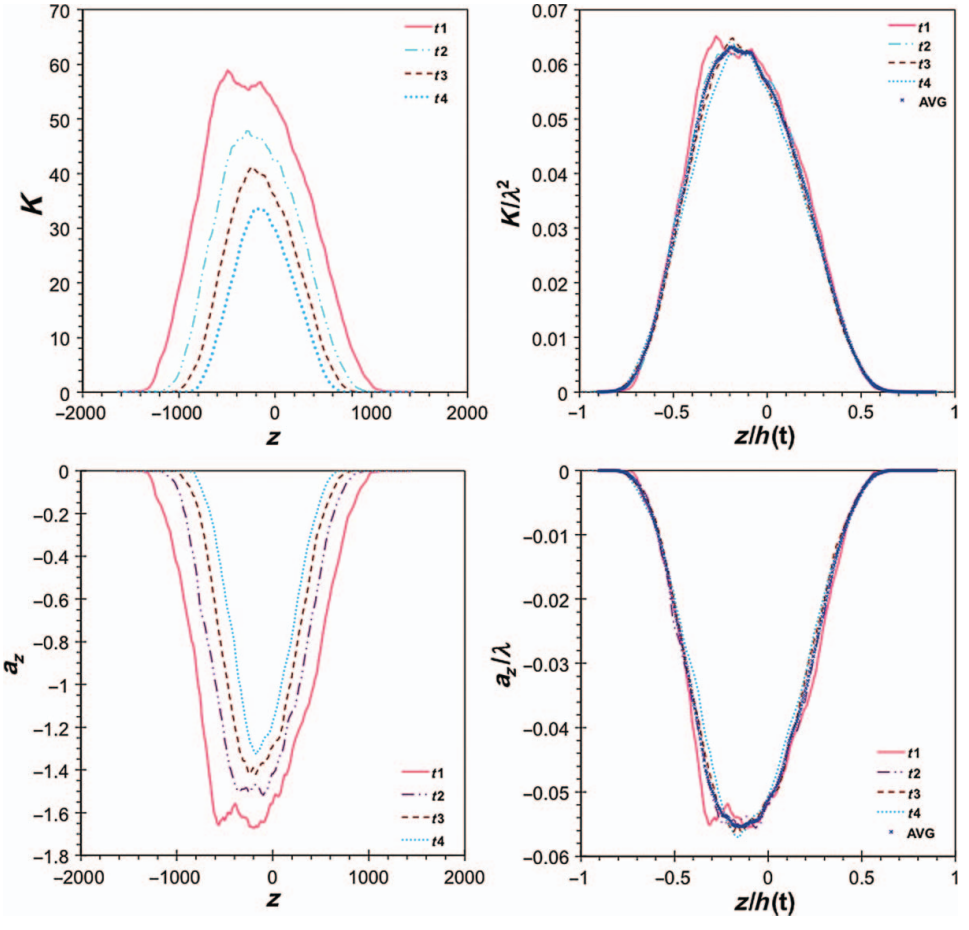

Figure 6. Actual RT DNS data (left) showing spatial and temporal growth; dimensionless RT DNS data that is invariant of temporal and spatial growth (right), $A = 0.5$. Legend: $t/\sqrt{l_0/|Ag|} = t1(31)$, $t2(27.5)$, $t3(25)$, $t4(22.5)$, where l_0 is the dominant initial wavelength of the perturbation [2].

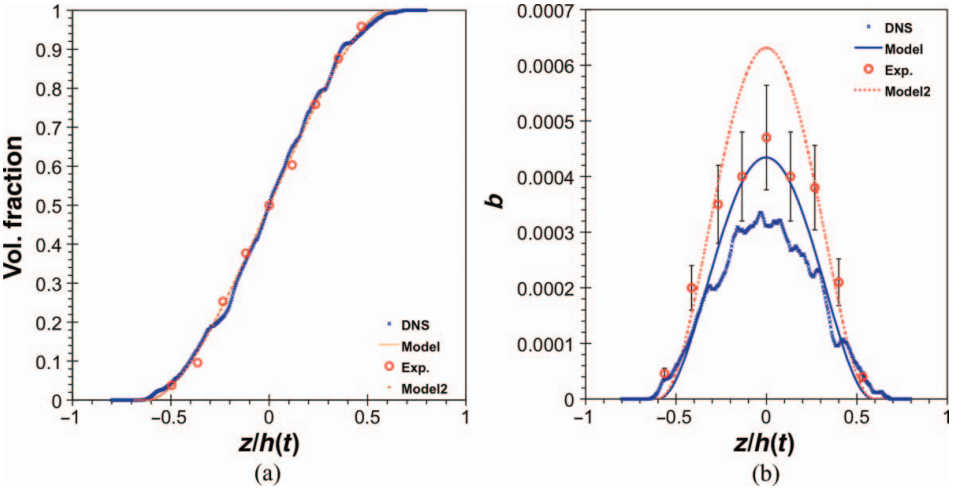

Figure 7. Direct comparison of (a) the volume fraction and (b) the density-specific-volume covariance produced by a second-moment closure model to DNS [3] and experimental data [27] for RT mixing, $A = 0.04$. The DNS and Model are compared in the self-similar region with $\alpha = 0.04$. The experiment (Exp.) and Model2 are compared in a non-self-similar region with $\alpha = 0.13$.

7.2.2 *Comparing the second-moment model to RT DNS at low Atwood*

The RT2 DNS set and the experimental data [27] are used to compare the model at a low Atwood number (0.04). The experimental data [27] report $\alpha \sim 0.13$, whereas DNS shows that the self-similar $\alpha \sim 0.04$ [3]. Although these differ by a factor of ~ 3, the model, DNS and experimental data agree on the volume fraction profile over the dimensionless mix width, shown in Figure 7(a). When comparing the density-specific-volume covariance (b), the experimental data over predict the DNS, shown in Figure 7(b). This over prediction is thought to be caused by the difference in growth rates, which may be caused by the effects of a low wave number in the experiments (current studies are underway to investigate these differences).

In order to avoid a direct comparison between the DNS and the experiment, the initial conditions were reconfigured to simulate a larger growth rate. The α of the model was altered by adjusting the initial value of the turbulent length scale until it was ~ 0.13 at 3.5 s (where the experimental data was captured) and referred to as Model2. The differences between Model and DNS and Model2 and Exp. are of similar magnitude. Overall, a reasonable agreement is seen between the model, experimental data, and DNS, despite the differences in α.

Comparisons of the mass-weighted turbulent velocity and the turbulent kinetic energy between DNS results, experimental data, and the second-moment model are shown in Figures 8 and 8(b), respectively. These quantities are not a direct comparison as they have been nondimensionalized by length and time scales $h(t)$ and $\sqrt{\alpha}t$, respectively. Still, reasonable agreement between the model, experimental, and DNS data are shown.

The Reynolds stress components are compared and shown in Figure 9(a). The model overpredicts the R_{33} component when compared to DNS data, whereas the R_{11} ($= R_{22}$) component agrees well with the DNS data. The overprediction in R_{33} could be due to the coefficient C_{rl} having an incorrect value, and $C_{\mathrm{rl}} = 0.4$ would provide a better match. However, improvements to the turbulence mass flux model may also show a better match

Downloaded by [the LANL Research Library] at 12:39 21 December 2011

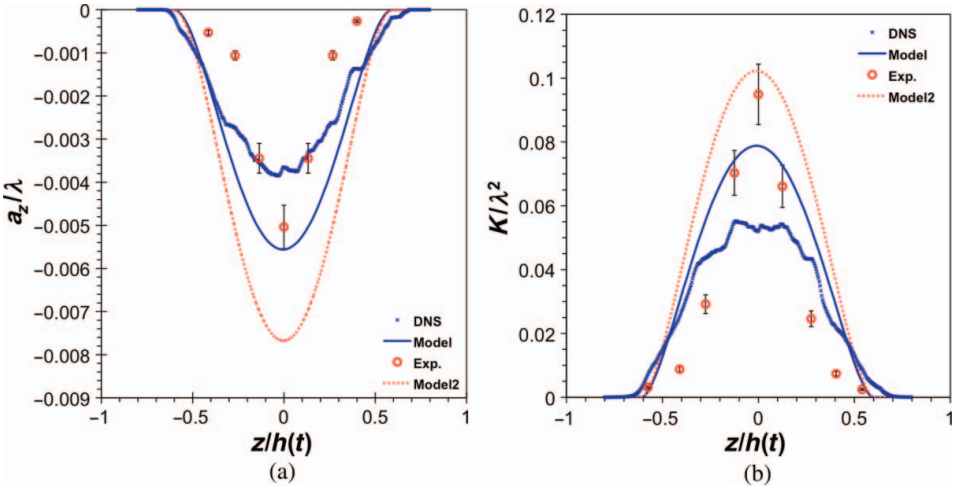

Figure 8. Comparison of (a) the dimensionless mass-weighted turbulent velocity and (b) the dimensionless turbulent kinetic energy produced by a second-moment model. The Model is compared to the DNS [3] in a self-similar region with $\alpha = 0.04$. The Model2 is compared to the experimental data [27] in a non-self-similar region with $\alpha = 0.13$. All the data are for $A = 0.04$.

between the Reynolds stress model and DNS. Since the match was reasonable, we chose to use the suggested coefficient and further investigated the effects of the destruction of the turbulent mass flux on a_i and R_{ij}. A comparison of the ratio of the streamwise and spanwise RMS velocities is also shown in Figure 9(b). Again, the DNS, model and experimental data agree rather well.

7.2.3 *Comparing the second-moment model to RT DNS at moderate Atwood*

The DNS data of Cabot and Cook [30], presented by Livescu et al. [2], are used to compare the model at a moderate Atwood number (0.5). Direct comparisons of the effects of mass and mixing are shown in Figure 10. The density profile compares very well with the DNS data while the second-moment model overpredicts the density-specific-volume covariance when compared to the DNS, similar to the low Atwood case.

Comparisons of the dimensionless Reynolds stress components and the turbulent kinetic energy are shown in Figure 11 (a) and (b). The model overpredicts the R_{33} component and agrees well with the R_{11} component, similar to the low Atwood case. The model also appears to capture the asymmetry or shift of the peak turbulent energy toward the spike side. This is primarily driven by the asymmetry found in both the turbulent mass flux and density-specific-volume covariance and a reason that the density-specific-volume covariance should be computed rather than the density variance which is only valid at low Atwood (i.e., the Boussinesq limit). The second-moment model compares well with the DNS predictions. Based on the simple decay model used, the dimensionless mass-weighted turbulent velocity also matches reasonably well with the moderate Atwood DNS, shown in Figure 11(c).

The turbulence length scale and dissipation are compared to DNS data and are shown in Figure 12. The dimensionless turbulent length scale compares well with the DNS data and is not only found to be about one-quarter of the mixing layer width but also a reasonable prediction of the asymmetry. The dissipation is modeled as $\varepsilon = K^{3/2}/S$, and the dimensionless dissipation shows to overpredict the DNS. This is thought to be due to the overprediction of the turbulent energy which is partly due to the overprediction in the turbulent mass flux.

Downloaded by [the LANL Research Library] at 12:39 21 December 2011

Downloaded by [the LANL Research Library] at 12:39 21 December 2011

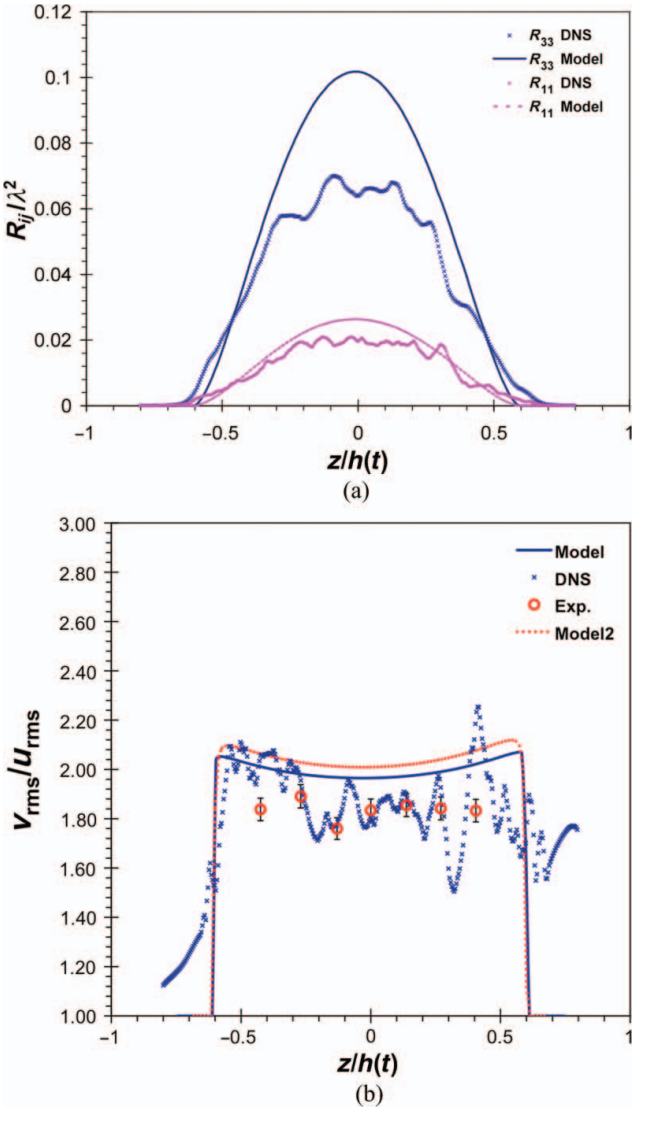

Figure 9. Comparison of (a) the dimensionless Reynolds stress components, and (b) the ratio of the root-mean-square (RMS) velocities. Model is compared to DNS data [3] in a self-similar region with $\alpha = 0.04$. Model2 is compared with experimental data [27] in a non-self-similar region with $\alpha = 0.13$. For all cases, $A = 0.04$.

The inverse turbulent time scale ($\sqrt{K}/S$) and inverse material or mix time scale ($\bar{\rho}\varepsilon_b/b$) are shown in Figure 13. These appear to be reasonable comparisons to DNS data.

7.2.4 Anisotropy

A true test of the Reynolds stress model (given in Equation (12)) is to compare the anisotropy. The dimensionless anisotropy tensor is defined as

$$b_{ij} = \frac{\tilde{R}_{ij}}{\tilde{R}_{kk}} - \frac{1}{3}\delta_{ij} \tag{49}$$

Downloaded by [the LANL Research Library] at 12:39 21 December 2011

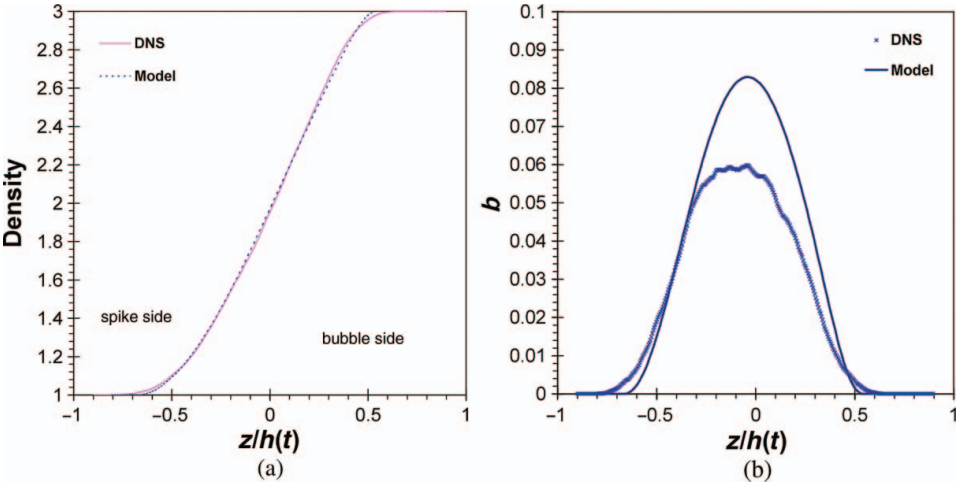

Figure 10. Direct comparison of (a) the second-moment model and DNS [2] for density and (b) the density-specific-volume covariance for 0.5 Atwood.

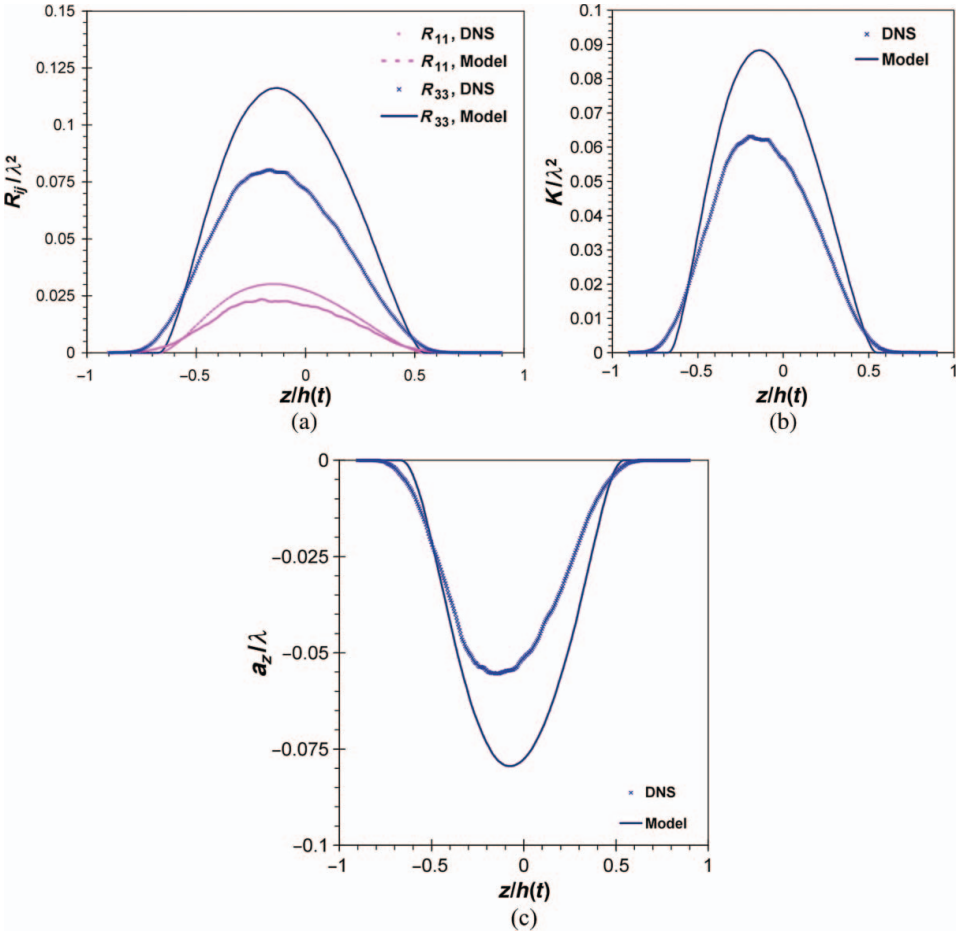

Figure 11. Comparison of second-moment model predictions with DNS [2] results for (a) Reynolds stress, (b) turbulent kinetic energy, (c) Favre-averaged turbulent velocity for 0.5 Atwood.

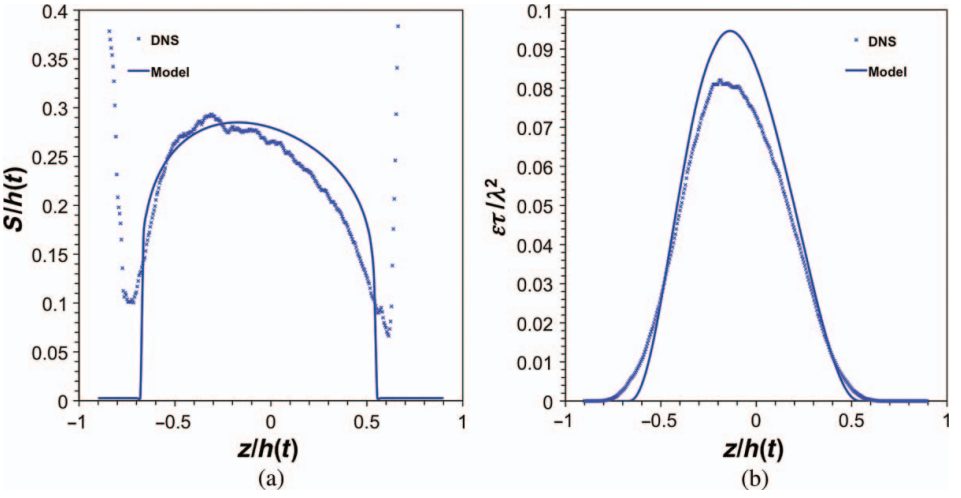

Figure 12. Comparison of second-moment model predictions with DNS [2] results for (a) turbulent length scale, and (b) turbulence dissipation for 0.5 Atwood.

with realizable limits $-1/3 < b_{ij} < 2/3$. The model proposed in Equation (11) adopted Daly and Harlow's [13] expression for the transport terms and assumed high-Reynolds-number flows such that the turbulent length scale is isotropic. The pressure strain terms were modeled by Rotta's [14] return to isotropy model and Naot et al.'s [15] *isotropization of production* (IP) model. These models are the simplest form and assume that an energy cascade exists.

A comparison of b_{33} for RT instabilities is shown in Figure 14 for low- and moderate Atwood numbers. The RT1 and RT2 datasets are shown for comparison. The model compares reasonably well for symmetrical, low Atwood data. However, at high Atwood values, a nonsymmetrical form develops over the mix width. The model poorly predicts

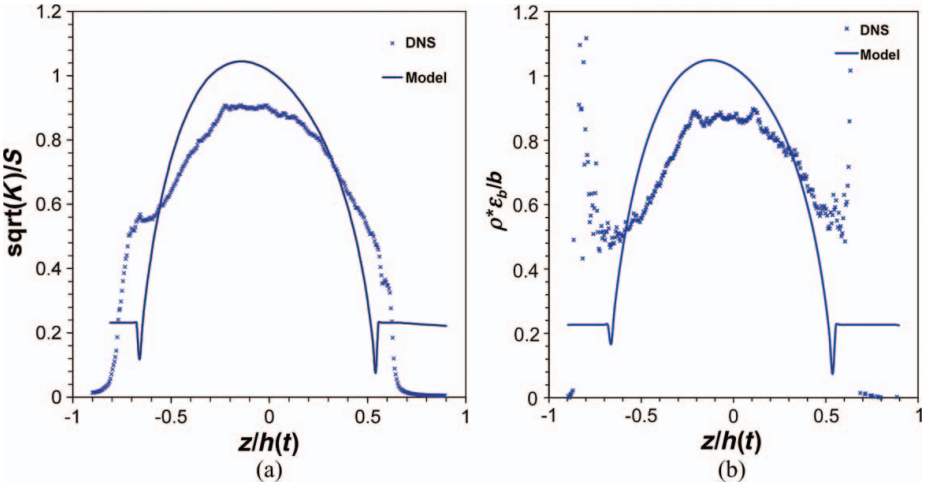

Figure 13. Comparison of (a) the dimensionless inverse turbulent time scale and (b) the inverse material or mix time scale for 0.5 Atwood.

Downloaded by [the LANL Research Library] at 12:39 21 December 2011

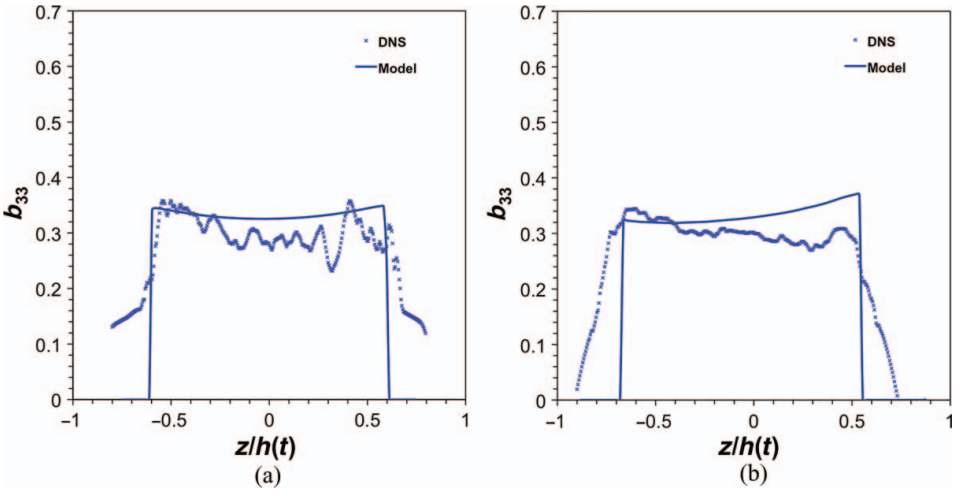

Figure 14. Comparison of the anisotropy in RT-type flows for low and moderate Atwood, (a) $A = 0.04$, and (b) $A = 0.5$. The prediction is compared to DNS [2].

the anisotropy on the bubble side. This could partly be due to the fact that the coefficient for the decay of a_i was assumed constant, when it really should be a factor of 2 greater on the outer edge of the bubble side (see Figure 3). This would suppress the main production mechanism in the transport equation for R_{ij}, and therefore a simple decay model to represent $\bar{\rho}\overline{v' P'_{,i}}$ warrants further studies. This is an example where one cannot criticize the models within R_{ij} until the additional quantities have adequate models. Currently, we are using the simplest/robust models available and documenting their strengths and weaknesses; future work is underway to improve on these models.

7.3 RM instability

The third application is the RM instability. Unlike the previous flows considered, this instability does not reach a self-similar form and, as a consequence, may challenge the turbulence models that were developed using this assumption. The RM instability arises when a shock is passed through an interface that separates two different density fluids, shown in Figure 1(c).

Poggi et al. [8] appeared to be the first to collect turbulence data within this type of mixing using laser Doppler anemometry (LDA). In this experiment, a vertical shock tube with a cross section of 8×8 cm^2 was used. The heavy fluid (SF6) was separated from the lighter fluid (air) using a thin membrane. A thin wire mesh was also placed above the membrane to help control the initial perturbation scales. The upward propagating shock (Mach $= 1.45$) created a mixing layer when it impacted the interface. After reshock, turbulence was evident. Poggi et al. [8] were able to seed the two fluids to obtain turbulent measurements within the mixing layer at moderate Atwood number (0.67). Since then, there have been no repeated attempts to verify this dataset.

Grègoire et al. [4] compared their second-order turbulence model to the experimental data of Poggi et al. [8]. The primary differences between their model and the present model are in modeling the second moment $\overline{v'\rho'}$ and using the turbulent length scale rather than dissipation. It is noted that there are no experimental data provided for $\overline{v'\rho'}$ or

Downloaded by [the LANL Research Library] at 12:39 21 December 2011

other production mechanisms such as $\overline{\rho' u'}/\bar{\rho}$ in RM-type flows, and therefore a detailed comparison is unavailable. This is one of the primary reasons of comparing these statistics to RT flows and then applying the calibrated results to RM flows. In this study, the coefficients were not calibrated or tuned for this type of instability. Thus, the model coefficients (shown in Table 2) were applied to RM instabilities.

The shock tube problem discussed above was set up as 1-D. The governing equations are ($R_{33} = R_{22}$):

Reynolds Stress:

$$\frac{\partial(\bar{\rho}\tilde{R}_{11})}{\partial t} + (\bar{\rho}\tilde{u}_1\tilde{R}_{11})_{,1} = 2(1 - C_{r1})\, a_1 \bar{P}_{,1} + 2\bar{\rho}(C_{r2} - 1)\,\tilde{R}_{11}\tilde{u}_{1,1} + C_r\left(\frac{S}{\sqrt{K}}\bar{\rho}\tilde{R}_{11}\tilde{R}_{11,1}\right)_{,1} - C_{r3}\bar{\rho}\frac{\sqrt{K}}{S}\left(\tilde{R}_{11} - \frac{1}{3}\tilde{R}_{kk}\right) - C_{r2}\frac{2}{3}\bar{\rho}\tilde{R}_{11}\tilde{u}_{1,1} + C_{r1}\frac{2}{3}a_1\bar{P}_{,1} - \bar{\rho}\frac{2}{3}\frac{K\sqrt{K}}{S}, \tag{50}$$

$$\frac{\partial\left(\bar{\rho}\tilde{R}_{22}\right)}{\partial t} = C_r\left(\frac{S}{\sqrt{K}}\bar{\rho}\tilde{R}_{11}\tilde{R}_{22,1}\right)_{,1} - C_{r3}\bar{\rho}\frac{\sqrt{K}}{S}\left(\tilde{R}_{22} - \frac{1}{3}\tilde{R}_{kk}\right) - C_{r2}\frac{2}{3}\bar{\rho}\tilde{R}_{11}\tilde{u}_{1,1} + C_{r1}\frac{2}{3}a_1\bar{P}_{,1} - \bar{\rho}\frac{2}{3}\frac{K\sqrt{K}}{S}. \tag{51}$$

Turbulent mass flux:

$$\frac{\partial(\bar{\rho}a_1)}{\partial t} + (\bar{\rho}\tilde{u}_1 a_1)_{,1} = b\bar{P}_{,1} - \tilde{R}_{11}\bar{\rho}_{,1} - \bar{\rho}a_1(\tilde{u}_1 - a_1)_{,1} + \bar{\rho}(a_1 a_1)_{,1} + \bar{\rho}C_a\left(\frac{S}{\sqrt{K}}\tilde{R}_{11}a_{1,1}\right)_{,1} - C_{a1}\bar{\rho}a_1\frac{\sqrt{K}}{S}. \tag{52}$$

Density-specific-volume covariance:

$$\frac{\partial(\bar{\rho}b)}{\partial t} + (\bar{\rho}\tilde{u}_1 b)_{,1} = 2\bar{\rho}a_1 b_{,1} - 2(b+1)\,a_1\bar{\rho}_{,1} + \bar{\rho}^2 C_b\left(\frac{S}{\bar{\rho}\sqrt{K}}\tilde{R}_{11}b_{,1}\right)_{,1} - C_{b1}\bar{\rho}b\frac{\sqrt{K}}{S}. \tag{53}$$

Turbulent length scale:

$$\frac{\partial(\bar{\rho}S)}{\partial t} + (\bar{\rho}\tilde{u}_1 S)_{,1} = -\frac{S}{K}\left(\frac{3}{2} - C_1\right)\bar{\rho}\tilde{R}_{11}\tilde{u}_{1,1} - \left(\frac{3}{2} - C_2\right)\bar{\rho}\sqrt{K} + C_s\left(\frac{S}{\sqrt{K}}\bar{\rho}\tilde{R}_{11}S_{,1}\right)_{,1} + \frac{S}{K}\left(\frac{3}{2} - C_3\right)a_1\bar{P}_{,1} - C_4\bar{\rho}S\bar{u}_{1,1}. \tag{54}$$

Species Concentration:

$$\frac{\partial(\bar{\rho}\tilde{c}^n)}{\partial t} + (\bar{\rho}\tilde{u}_1\tilde{c}^n)_{,1} = \left(C_c\frac{S}{\sqrt{K}}\bar{\rho}\tilde{R}_{11}\tilde{c}^n_{,1}\right)_{,1}. \tag{55}$$

Downloaded by [the LANL Research Library] at 12:39 21 December 2011

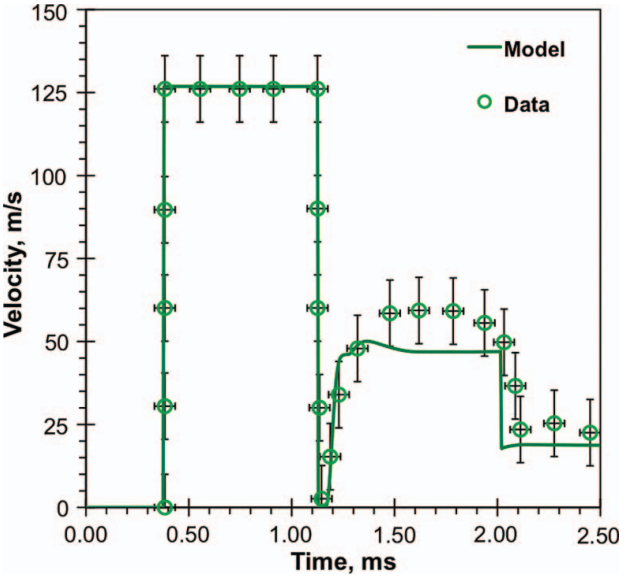

Figure 15. Comparison of velocity profile at 161 mm from the initial interface. Data are given in Poggi et al. [8].

The above-modeled equations are applied to the experiment of Poggi et al. [8], described above. The velocity is compared with the experimental data and shown in Figure 15. The velocity difference between the model and experiment at the second plateau is attributed to turbulent boundary layer effects, where an acceleration of the fluid is seen in the experiments [8]. Boundary layer effects were not accounted for in this model; however, Mügler and Gauthier [36] showed that the data and experiments match rather well when these effects are considered. Overall, the model agrees reasonably well with the velocity data.

The Favre-averaged Reynolds stresses can be converted to Reynolds-averaged by the following relationship:

$$\overline{u_i'u_j'} = \tilde{R}_{ij} + a_i a_j - \frac{\overline{\rho' u_i' u'}_j}{\bar{\rho}}. \tag{56}$$

The last two terms in the above equation should be of the same order, which was determined as ∼1% of the Favre-averaged Reynolds stress and therefore the last two terms are neglected in the following comparisons.

During the simulation of the data of Poggi et al. [8], it was found that the value for the coefficient $C_4 = 0$ produced a high axial Reynolds stress, but by including the compressibility term ($-C_4\bar{\rho}S\bar{u}_{j,j}$, shown in Eqn. (54) and in Ref. [6]) in the length scale equation (discussed in §3.2) with the coefficient $C_4 = -1.2$, a reasonable agreement between the simulation and experimental data was achieved. A comparison of R_{11} over time is shown in Figure 16. At positions 161 and 178.5 mm beyond the initial interface, which is in the decay region after the first shock but before reshock, the model compares reasonably well with the experimental data. Poggi et al. [8] showed additional data at 51 and 125 mm beyond the initial interface, and although not shown here, the current model underpredicts this data, similar to [4]. The spike in R_{11}, between 1.85 and 1.9 ms (at 178.5 mm), is due to the second

Downloaded by [the LANL Research Library] at 12:39 21 December 2011

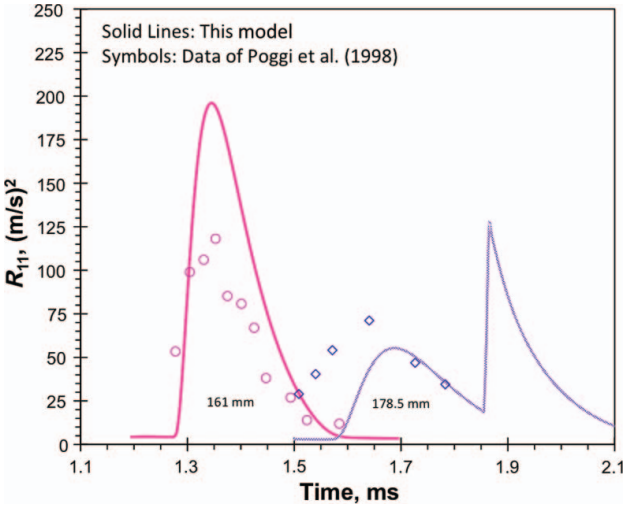

Figure 16. Second-moment model compared to axial Reynolds stress data from the CEA shock tube experiment [2].

reshock. Overall, a reasonable agreement is seen between the model and experimental data.

Data for the Reynolds stress anisotropy at 169 mm are found in [4]. Here, the model is compared with the data and shown in Figure 17. The two components compare reasonably well with the data, although much of the data in the transverse direction are within the measurement noise.

An important factor in this experiment is the growth rate of the mixing layer. The interface of air and SF6, based on a 1% concentration level, is plotted and compared with the experimental data, shown in Figure 18. The model compares reasonably well with the experimental data after the first shock. However, it underpredicts the measured growth after the second reshock.

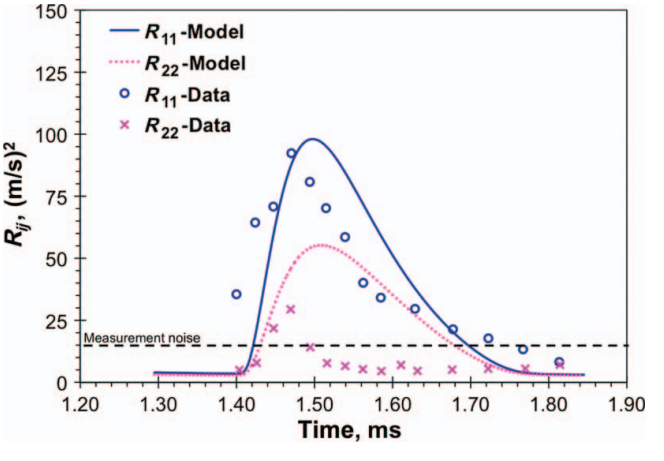

Figure 17. Comparison of the Reynolds stress components to the experimental data of CEA shock tube experiment (data found in [4, 8]). Measurement position is 169 mm beyond the initial interface.

Downloaded by [the LANL Research Library] at 12:39 21 December 2011

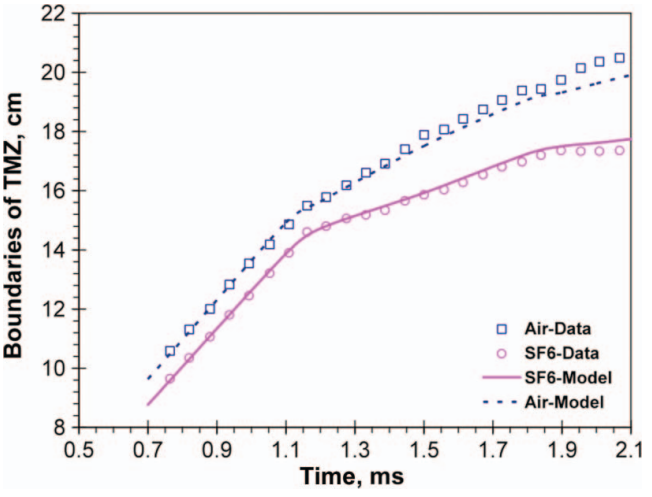

Figure 18. Prediction of the turbulent mixing zone (TMZ) boundaries by a second-moment model and compared to the measured data of Poggi et al. [8].

8. Summary and conclusions

A set of higher order closure equations for a second-moment model, originally derived by Besnard et al. (1992), was further developed and applied to a broad set of single-phase and variable density turbulence data, spanning from free shear flow to shock-induced mixing. This second-moment closure includes higher order closures, namely, the turbulent mass flux and the density-specific-volume covariance. Other works involving higher order closures simplify the density-specific-volume covariance to the Boussinesq limit.

In this study, we document several strengths and areas of improvement for the second-moment closure applied to single and variable density flows:

1. First, we illustrate that the Boussinesq limit for the density-specific-volume covariance is not appropriate for high Atwood instabilities. Instead of modeling the density variance, a model was proposed for the density-specific-volume covariance based on the work of Besnard et al. (1992). At moderate Atwood number Rayleigh–Taylor flows, the model does show asymmetry with the peak values of the density-specific-volume covariance occurring on the lighter side of the fluid interface, similar to DNS.
2. To improve on the asymmetry, an exact equation for the destruction term of the density-specific-volume covariance was derived and presented. However, the necessary data needed to further develop this equation was found to be limited (current efforts to obtain this data are underway). Therefore, a simple decay model was adopted and the coefficients for this model were calibrated to the exact terms found in DNS of Rayleigh–Taylor instabilities. This calibration showed that the decay coefficient was constant across the mixing layer.
3. It was also found during the calibration process that a simple decay model is not appropriate for the destruction rate of the turbulence mass flux in Rayleigh–Taylor flows. The coefficient shows a wide variation over the mix width and can differ by as much as a factor of 2 near the outer edges of the mixing zone. This appears to be inconsistent with the suggested values found in previous literature.

Downloaded by [the LANL Research Library] at 12:39 21 December 2011

4. In single-phase shear flow, the value of $C_1 = 1.44$, within the turbulent length scale equation, underpredicted the Reynolds stress components and the growth rate of the experimental data and DNS. Decreasing this value to 1.2 showed a better comparison of the Reynolds stress components and growth rate between the model, experimental data, and DNS. However, contrary to the data, the modeled form of the pressure strain terms within the Reynolds stress equation does not appear to capture the proper anisotropy within the diagonal components, but it does capture the shear component.
5. The model coefficients were calibrated to single-phase shear and variable density Rayleigh–Taylor experiments/DNS. The model was then applied to a shock tube and compared to the experimental data measured by Poggi et al. [8]. The purpose of this exercise was to understand if the model could capture the effect of a completely different type of flow that was not used during the calibration process. Overall, the model does a reasonable job at capturing the anisotropy in the Reynolds stress and the mix width after the first reshock when the compressibility term is included in the turbulence length scale equation with $C_4 = -1.2$; implying that this term should not be neglected in shocked flows. However, additional data are needed to compare mix quantities in this flow regime.

The second-moment model presented in this study was compared to DNS and experimental data for SD, Rayleigh–Taylor, and RM instabilities. These comparisons include Reynolds stress components and anisotropy, turbulent and material mixing time scales, density-specific-volume covariance, turbulent length scale and dissipation, growth rates and mix widths, turbulent mass flux and mean velocity profiles, turbulent kinetic energy, and density variation and volume fraction. This model is considered an improvement over previously developed models, which use turbulent viscosity [6, 7] and density variance [4]. Overall, the second-moment model for variable density turbulence compares well with DNS and experimental data. Future work to improve this model should focus on developing models for the destruction of the density-specific-volume covariance and turbulent mass flux along with improving the pressure strain model and developing transport equations for nonisotropic dissipation or turbulent length scale.

Acknowledgements

This work was supported by the U.S. Department of Energy, subcontract #DE-AC52-06NA25396.

References

[1] D. Livescu, and J.R. Ristorcelli, *Variable-density mixing in buoyancy-driven turbulence*, J. Fluid Mech. *605* (2008), p. 145.
[2] D. Livescu, J.R. Ristorcelli, R.A. Gore, S.H. Dean, W.H. Cabot, and A.W. Cook, *High-Reynolds number Rayleigh–Taylor turbulence*, J. Turbul. *10* (2009), p. 1.
[3] D. Livescu, J.R. Ristorcelli, M.R. Petersen, and R.A. Gore, *New phenomena in variable-density Rayleigh–Taylor turbulence*, Phys. Scr. *T142* (2010), p. 014015.
[4] O. Grégoire, D. Souffland, and S. Gauthier, *A second-order turbulence model for gaseous mixtures induced by Richtmyer–Meshkov instability*, J. Turbul. *6* (2005), p. 1.
[5] D. Besnard, F.H. Harlow, R.M. Rauenzahn, and C. Zemach, *Turbulence Transport Equations for Variable-Density Turbulence and Their Relationship to Two-Field Models, LA-UR-12303*, Los Alamos National Laboratory, Los Alamos, NM, 1992.
[6] A. Banerjee, R.A. Gore, and M.J. Andrews, *Development and validation of a turbulent-mix model for variable-density and compressible flows*, Phys. Rev. E *82* (2010), p. 046309.
[7] K. Stalsberg-Zarling and R.A. Gore, *The BHR2 Turbulence Model: Incompressible Isotropic Decay, Rayleigh–Taylor, Kelvin–Helmholtz and Homogeneous Variable Density Turbulence, LA-UR 11-04773*, Los Alamos National Laboratory, Los Alamos, NM, 2011.

Downloaded by [the LANL Research Library] at 12:39 21 December 2011

[8] F. Poggi, M.-H. Thorembey, and G. Rodriguez, *Velocity measurements in turbulent gaseous mixtures induced by Richtmyer–Meshkov instability*, Phys. Fluids *10* (1998), p. 2698.
[9] V.A. Andronov, S.M. Barkhrakh, E.E. Meshkov, V.V. Nikiforov, A.V. Pevnitskii, and A.I. Tolshmyakov, *An experimental investigation and numerical modeling of turbulent mixing in one-dimensional flows*, Sov. Phys. Doklady *27* (1982), p. 393.
[10] F.A. Williams, *Combustion Theory*, 2nd ed., Addison-Wesley, Reading, MA, 1985.
[11] A.W. Cook, *Enthalpy diffusion in multicomponent flows*, Phys. Fluids *21* (2009), p. 055109.
[12] T. Cebeci and A.M.O. Smith, *Analysis of Turbulent Boundary Layers, Series: Applied Mathematics and Mechanics*, Academic Press, New York, 1974.
[13] B.D. Daly and F.H. Harlow, *Transport equations in turbulence*, Phys. Fluids *13* (1970), p. 2634.
[14] J.C. Rotta, *Statistische theorie nichthomogener turbulenz*, Z. Phys. *129* (1951), p. 547 (an English translation can be found in NASA-TT-F-14560, Oct. 1972).
[15] D. Naot, A. Shavit, and M. Wolfshtein, *Interactions between components of the turbulent velocity correlation tensor due to pressure fluctuations*, Israel J. Technol. *8* (1970), p. 259.
[16] B.E. Launder, G.J. Reese, and W. Rodi, *Progress in the development of a Reynolds-stress turbulence closure*, J. Fluid Mech. *68* (1975), p. 537.
[17] S. Banerjee, Ö. Ertunç, Ç. Köksoy, and F. Durst, *Pressure strain rate modeling of homogeneous axisymmetric turbulence*, J. Turbul. *10* (2009), p. 1.
[18] J. Luo, and B. Lakshminarayana, *Prediction of strongly curved turbulent duct flows with Reynolds stress model*, AIAA J. *35* (1997), p. 91.
[19] S. Gauthier and M. Bonnet, *A k–ε model for turbulent mixing in shock-tube flows induced by Rayleigh–Taylor instability*, Phys. Fluids A, *2*, 9 (1990), p. 1685.
[20] W.C. Reynolds, *Fundamentals of Turbulence for Turbulence Modeling and Simulation, Lecture Notes for Von Karman Institute, AGARD Lecture Series No. 86*, NATO, New York, 1987.
[21] S.B. Pope, *Turbulent Flows*, Cambridge University Press, New York, 2000.
[22] G. Dimonte and R. Tipton, *K–L turbulence model for the self-similar growth of the Rayleigh–Taylor and Richtmyer–Meshkov instabilities*, Phys. Fluids *18* (2006), p. 085101.
[23] P.S. Bernard and J.M. Wallace, *Turbulent Flow: Analysis, Measurement and Prediction*, Wiley and Sons, New York, 2002.
[24] J.H. Bell and R.D. Mehta, *Development of a two-stream mixing layer from tripped and untripped boundary layers*, AIAA J. *28* (1990), p. 2034.
[25] M.M. Rogers and R.D. Moser, *Direct simulation of a self-similar turbulent mixing layer*, Phys. Fluids *6* (1994), p. 903.
[26] B.E. Launder, *Second-moment closure: Present. . .and future?*, Int. J. Heat Fluid Flow *10* (1989), p. 282.
[27] A. Banerjee, W.N. Kraft, and M.J. Andrews, *Detailed measurements of a statistically steady Rayleigh–Taylor mixing layer from small to high Atwood numbers*, J. Fluid Mech. *659* (2010), p. 127.
[28] J.R. Ristorcelli and T.T. Clark, *Rayleigh–Taylor turbulence: Self-similar analysis and direct numerical simulations*, J. Fluid Mech. *507* (2004), p. 213.
[29] J.D. Schwarzkopf, C.T. Crowe, and P. Dutta, *Application of a volume averaged k–ε model to particle-laden turbulent channel flow*, J. Fluids Eng. *131* (2009), p. 101301.
[30] W.H. Cabot and A.W. Cook, *Reynolds number effects on Rayleigh–Taylor instability with possible implications for type-1a supernovae*, Nat. Phys. *2* (2006), p. 562.
[31] E. Ruffin, R. Schiestel, F. Anselmet, M. Amielh, and L. Fulachier, *Investigation of characteristic scales in variable density turbulent jets using a second order model*, Phys. Fluids *6* (1994), p. 2785.
[32] P. Chassaing, *The modeling of variable density turbulent flows,* Flow, Turbulence and Combustion *66* (2001), p. 293.
[33] M.J. Andrews and D.B. Spalding, *A simple experiment to investigate two-dimensional mixing by Rayleigh–Taylor instability*, Phys. Fluids A, *2*, 6 (1990), p. 922.
[34] M. Gittings, R. Weaver, M. Clover, T. Betlach, N. Byrne, R. Coker, E. Dendy, R. Hueckstaedt, K. New, W.R. Oakes, D. Ranta, and R. Stefan, *The RAGE radiation-hydrodynamic code*, Comp. Sci. Disc. *1* (2008), p. 015005.
[35] D.P. Young, R.G. Melvin, M.B. Bieterman, F.T. Johnson, S.S. Samant, and J.E. Bussoletti, *A locally refined rectangular grid finite element method: Application to computational fluid dynamics and computational physics*, J. Comput. Phys. *92* (1991), p. 1.
[36] C. Mügler and S. Gauthier, *Two-dimensional Navier–Stokes simulations of gaseous mixtures induced by Richtmyer–Meshkov instability*, Phys. Fluids *12* (2000), p. 1783.

Downloaded by [the LANL Research Library] at 12:39 21 December 2011

Downloaded by [the LANL Research Library] at 12:39 21 December 2011

Appedix

A.1 Exact Euler equations for variable density turbulence

Continuity:

$$\frac{\partial \bar{\rho}}{\partial t} + (\bar{\rho}\tilde{u}_j)_{,j} = 0.$$

Momentum:

$$\frac{\partial (\bar{\rho}\tilde{u}_i)}{\partial t} + \left(\bar{\rho}\tilde{u}_i\tilde{u}_j + \bar{P}\delta_{ij} + \bar{\rho}\tilde{R}_{ij}\right)_{,j} = \bar{\rho}g_i.$$

Energy:

$$\frac{\partial}{\partial t}(\bar{\rho}\tilde{E}) + (\bar{\rho}\tilde{u}_j\tilde{E})_{,j} = -(\bar{P}\bar{u}_j)_{,j} - (\bar{\rho}\tilde{u}_i\tilde{R}_{ij})_{,j} - \left(\overline{P'u'_j}\right)_{,j} - \left(\overline{\rho I''u''_j}\right)_{,j} - \frac{1}{2}\left(\overline{\rho u''_i u''_i u''_j}\right)_{,j} - \bar{q}^d_{j,j}.$$

Species mass fraction:

$$\frac{\partial (\bar{\rho}\tilde{c}^n)}{\partial t} + \left(\bar{\rho}\tilde{u}_j\tilde{c}^n\right)_{,j} = -\left(\overline{\rho u''_j c''^m}\right)_{,j}.$$

Turbulence Reynolds stress:

$$\begin{aligned}\frac{\partial(\bar{\rho}\tilde{R}_{ij})}{\partial t} + \frac{\partial}{\partial x_k}(\bar{\rho}\tilde{u}_k\tilde{R}_{ij}) = {} & a_i\frac{\partial \bar{P}}{\partial x_j} + a_j\frac{\partial \bar{P}}{\partial x_i} - \bar{\rho}\tilde{R}_{ik}\frac{\partial \tilde{u}_j}{\partial x_k} - \bar{\rho}\tilde{R}_{jk}\frac{\partial \tilde{u}_i}{\partial x_k} - a_i\frac{\partial \tilde{\tau}_{jk}}{\partial x_k} - a_j\frac{\partial \tilde{\tau}_{ik}}{\partial x_k} \\ & - \frac{\partial}{\partial x_k}\overline{\rho u''_i u''_j u''_k} + \frac{\partial}{\partial x_k}\left(\overline{u''_i\tau''_{jk}} + \overline{u''_j\tau''_{ik}}\right) - \frac{\partial}{\partial x_j}\overline{u''_i P'} - \frac{\partial}{\partial x_i}\overline{u''_j P'} \\ & + \overline{P'\frac{\partial u''_i}{\partial x_j}} + \overline{P'\frac{\partial u''_j}{\partial x_i}} - \overline{\tau''_{jk}\frac{\partial u''_i}{\partial x_k}} - \overline{\tau''_{ik}\frac{\partial u''_j}{\partial x_k}}.\end{aligned}$$

Turbulence mass flux:

$$\begin{aligned}\frac{\partial (\bar{\rho}a_i)}{\partial t} + (\bar{\rho}\tilde{u}_k a_i)_{,k} = {} & b\left(\bar{P}_{,i} - \bar{\tau}_{ki,k}\right) - \tilde{R}_{ik}\bar{\rho}_{,k} + \bar{\rho}\left(a_k a_i\right)_{,k} - \bar{\rho}a_k\bar{u}_{i,k} - \bar{\rho}\left(\frac{\overline{\rho' u'_i u'_k}}{\bar{\rho}}\right)_{,k} \\ & + \bar{\rho}\overline{\upsilon'\left(P'_{,i} - \tau'_{ki,k}\right)}.\end{aligned}$$

Density-specific-volume covariance:

$$\frac{\partial (\bar{\rho}b)}{\partial t} + (\bar{\rho}b\tilde{u}_k)_{,k} = -2(b+1)a_k\bar{\rho}_{,k} + 2\bar{\rho}a_k b_{,k} + \bar{\rho}^2\left(-\frac{\overline{\rho'\upsilon' u'_k}}{\bar{\rho}}\right)_{,k} - 2\bar{\rho}^2\varepsilon_b.$$

Dissipation of density-specific-volume covariance:

$$\begin{aligned}\frac{\partial}{\partial t}(\bar{\rho}\varepsilon_b) + \left(\bar{\rho}\varepsilon_b\tilde{u}_j\right)_{,j} = {} & \bar{\rho}\overline{\upsilon'\frac{\partial d}{\partial t}} + \bar{\rho}\bar{u}_j\overline{\upsilon' d_{,j}} - \bar{\rho}a_j\varepsilon_{b,j} + \bar{\rho}\varepsilon_b a_{j,j} + \bar{\rho}\varepsilon_b\tilde{u}_{j,j} \\ & - \bar{\rho}\bar{\upsilon}_{,j}\overline{u'_j d} - \bar{\rho}\overline{\left(\upsilon' u'_j d\right)}_{,j} + \bar{\rho}\overline{u'_j\upsilon' d_{,j}} + \bar{\rho}\bar{\upsilon}\overline{d^2} + 2\bar{\rho}\overline{\upsilon' d^2}.\end{aligned}$$

Downloaded by [the LANL Research Library] at 12:39 21 December 2011

A.2 Modeled form of the Euler equations for variable density turbulence

Continuity:

$$\frac{\partial \bar{\rho}}{\partial t} + (\bar{\rho}\tilde{u}_j)_{,j} = 0.$$

Momentum:

$$\frac{\partial (\bar{\rho}\tilde{u}_i)}{\partial t} + (\bar{\rho}\tilde{u}_i\tilde{u}_j + \bar{P}\delta_{ij} + \bar{\rho}\tilde{R}_{ij})_{,j} = \bar{\rho}g_i.$$

Total energy:

$$\frac{\partial}{\partial t}\left(\bar{\rho}\tilde{E}\right) + (\bar{\rho}\tilde{u}_j\tilde{E})_{,j} = -(\bar{P}\tilde{u}_j)_{,j} - \left(\tilde{u}_i\bar{\rho}\tilde{R}_{ij}\right)_{,j} + \left(\bar{\rho}\tilde{R}_{ij}\frac{S}{\sqrt{K}}\left[C_k K_{,j} + C_e\frac{C_v}{\mathrm{Pr}_t}\tilde{T}_{,j} + C_c\bar{h}^n\tilde{c}^n_{,j}\right]\right)_{,i}.$$

Species mass fraction:

$$\frac{\partial (\bar{\rho}\tilde{c}^n)}{\partial t} + (\bar{\rho}\tilde{u}_j\tilde{c}^n)_{,j} = \left(C_c\frac{S}{\sqrt{K}}\bar{\rho}\tilde{R}_{jm}\tilde{c}^n_{,m}\right)_{,j}.$$

Turbulence Reynolds stress:

$$\begin{aligned}\frac{\partial\left(\bar{\rho}\tilde{R}_{ij}\right)}{\partial t} + \left(\bar{\rho}\tilde{u}_k\tilde{R}_{ij}\right)_{,k} &= (1-C_{r1})\left[a_i\bar{P}_{,j} + a_j\bar{P}_{,i}\right] + \bar{\rho}\,(C_{r2}-1)\left[\tilde{R}_{ik}\tilde{u}_{j,k} + \tilde{R}_{jk}\tilde{u}_{i,k}\right]\\ &\quad + C_r\left(\frac{S}{\sqrt{K}}\bar{\rho}\tilde{R}_{kn}\tilde{R}_{ij,n}\right)_{,k} - C_{r3}\bar{\rho}\frac{\sqrt{K}}{S}\left(\tilde{R}_{ij} - \frac{1}{3}\tilde{R}_{kk}\delta_{ij}\right)\\ &\quad - C_{r2}\frac{2}{3}\bar{\rho}\tilde{R}_{mk}\tilde{u}_{m,k}\delta_{ij} + C_{r1}\frac{2}{3}a_k\bar{P}_{,k}\delta_{ij} - \bar{\rho}\frac{2}{3}\frac{K\sqrt{K}}{S}\delta_{ij}.\end{aligned}$$

Turbulence length scale:

$$\begin{aligned}\frac{\partial(\bar{\rho}S)}{\partial t} + \left(\bar{\rho}\tilde{u}_j S\right)_{,j} &= -\frac{S}{K}\left(\frac{3}{2} - C_1\right)\bar{\rho}\tilde{R}_{ij}\tilde{u}_{i,j} + C_s\left(\frac{S}{\sqrt{K}}\bar{\rho}\tilde{R}_{kn}S_{,n}\right)_{,k}\\ &\quad - \left(\frac{3}{2} - C_2\right)\bar{\rho}\sqrt{K} + \frac{S}{K}\left(\frac{3}{2} - C_3\right)a_j\bar{P}_{,j} - C_4\bar{\rho}S\bar{u}_{j,j}.\end{aligned}$$

Turbulence mass flux:

$$\begin{aligned}\frac{\partial(\bar{\rho}a_i)}{\partial t} + (\bar{\rho}\tilde{u}_k a_i)_k &= b\bar{P}_{,i} - \tilde{R}_{ik}\bar{\rho}_{,k} - \bar{\rho}a_k(\tilde{u}_i - a_i)_{,k} + \bar{\rho}\,(a_k a_i)_{,k}\\ &\quad + \bar{\rho}C_a\left(\frac{S}{\sqrt{K}}\tilde{R}_{kn}a_{i,n}\right)_{,k} - C_{a1}\bar{\rho}\frac{\sqrt{K}}{S}a_i.\end{aligned}$$

Density-specific-volume covariance:

$$\frac{\partial(\bar{\rho}b)}{\partial t} + (\bar{\rho}b\tilde{u}_k)_{,k} = -2\,(b+1)\,a_k\bar{\rho}_{,k} + 2\bar{\rho}a_k b_{,k} + \bar{\rho}^2 C_b\left(\frac{S}{\bar{\rho}\sqrt{K}}\tilde{R}_{mn}b_{,n}\right)_{,m} - C_{b1}\bar{\rho}\frac{\sqrt{K}}{S}b.$$

The mean temperature is determined from the caloric equation of state $\tilde{I} = C_v\tilde{T}$, with $\tilde{I} = \tilde{E} - \frac{1}{2}\bar{\rho}\tilde{u}_i\tilde{u}_i - K$, and the mean pressure is given by the ideal-gas equation of state, $\bar{P} = (1-\gamma)\,\bar{\rho}\tilde{I}$.